iScience

CellPress

Article

# Synchronous Healing of Li Metal Anode via Asymmetrical Bidirectional Current

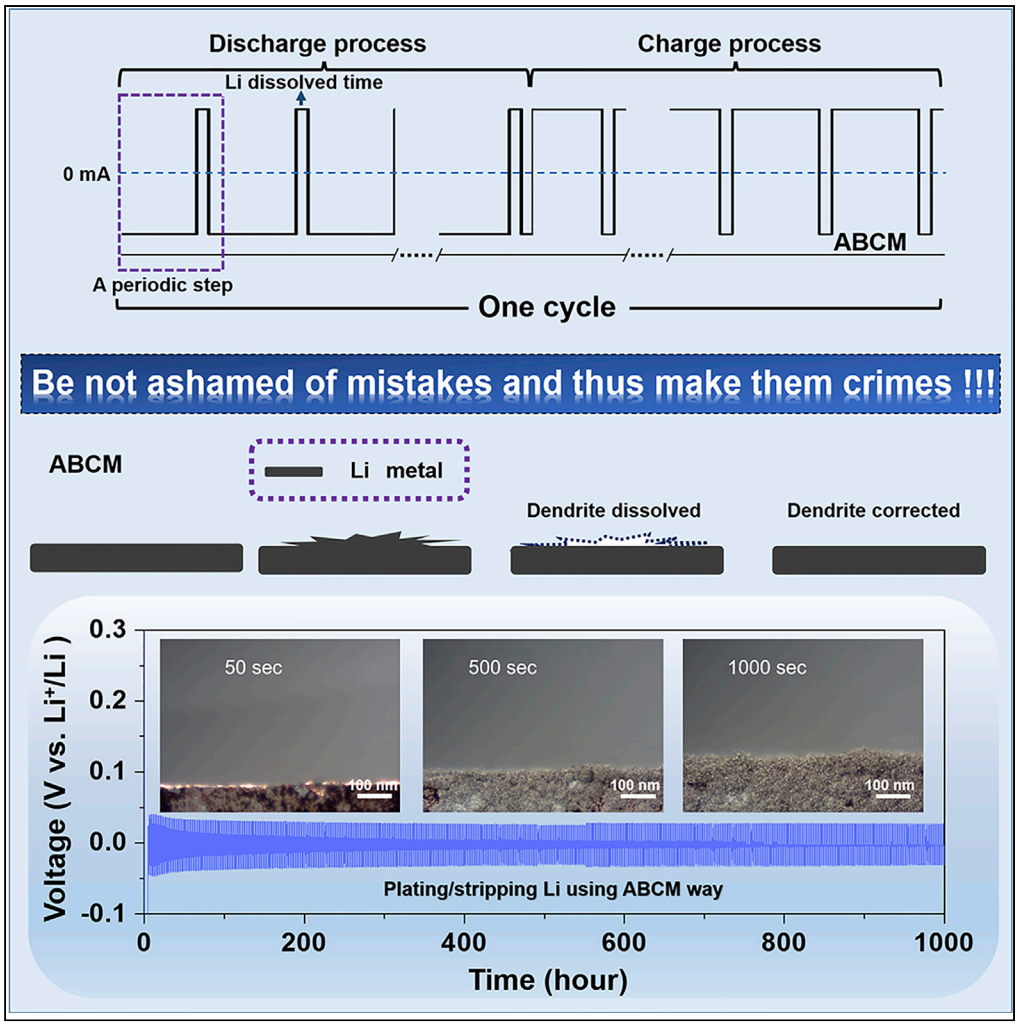


Dong Wang, Chichu Qin, Xilong Li, ..., Mengyang Cao, Lu Huang, Yingpeng Wu

wuyingpeng@hnu.edu.cn

## HIGHLIGHTS

A healable Li metal anode via anti-direction current to correct dendrite timely

Suppressed dendrite growth, very low and stable polarization after long cycling

Technology for stable Li metal battery without any chemical/physical modification

Wang et al., iScience *23*, 100781
January 24, 2020 
https://doi.org/10.1016/j.isci.2019.100781

iScience

CellPress

Article

# Synchronous Healing of Li Metal Anode via Asymmetrical Bidirectional Current

Dong Wang,[1,2] Chichu Qin,[1,2] Xilong Li,[1] Ganqiang Song,[1] Yumin Liu,[1] Mengyang Cao,[1] Lu Huang,[1] and Yingpeng Wu[1,3,*]

## SUMMARY

**The creation of Li metal anodes while minimizing dendrite growth is an important challenge for developing high-energy density batteries. Dendrites can originate from an inhomogeneous charge distribution or an irregular substrate, and often, the way to suppress dendrite growth is to avoid their formation altogether (ion-uniform mechanism over a shelf time). Herein, we propose a different route to eliminate dendrite formation, called an asymmetrical bidirectional current mode (ABCM) of charging, leading to a healable Li metal anode and resulting in a positive feedback cycle. This mode allows for a stable cyclic performance and suppresses dendrite formation effectively (while holding the polarization ~27 mV for over 1,000 h), and provides a better result than suppressing Li dendrites via weakening of the Li dendrite (ion-uniform mechanism). These results indicate that ABCM may be a promising way to stabilize the Li anode of Li metal batteries, without any chemical/physical modification of the anode.**

## INTRODUCTION

Li metal is a promising candidate for the anode of next-generation high-energy-density battery (Deng et al., 2019; Liang et al., 2017; Lin et al., 2017; Zhang et al., 2020). A stable Li metal anode is a key point for the practical application of Li metal battery (LMB) (Cheng et al., 2017; Lu et al., 2014; Qiao et al., 2017; Zhang et al., 2018). Therefore, explorations on non-dendrite anode and reducing dead Li are eagerly required, such as high-modulus SEI film coating on Li metal (Liu et al., 2019a; Shi et al., 2018; Wang et al., 2017b), high-surface-energy substrate (Hou et al., 2019; Wang et al., 2017a), low local current density (Zhang et al., 2017), more reaction sites (Yang et al., 2015), cross-linking film (Zhao et al., 2019), and so on (Liang et al., 2019; Westover et al., 2019; Xu et al., 2019). However, once the uncontrollable dendrite occurs, the negative feedback cycle (SEI broken, dendrite worsen and so on) that follows would cause Li metal anode's failure quickly. To overcome such problem, healable anodes are rising recently to suppress inducing-dendrite issues, by the methods such as optimized charge distribution or thermodynamic nucleation (Huang et al., 2018; Hundekar et al., 2019; Zhu et al., 2019). Ding et al. proposed healable Li metal anode via $Cs^+$ additive with electrostatic shield mechanism (Ding et al., 2013). Li et al. proposed healable anode via heating-induced nucleation affection (Li et al., 2018a). Meanwhile, an appropriate stress distribution also can lead to a healing behavior with a zipper-like-SEI mechanism (Wang et al., 2018a, 2018c).

As we know, the surface charge distribution of Li metal is highly affected by extra filed force, such as Lorentz force and external power supply (Li et al., 2018b; Shen et al., 2019; Wang et al., 2019). Therefore, we can regulate the charge distribution via programming charge-discharge mode (Liang et al., 2019; Yang et al., 2014). For example, inducing external alternating current could enhance the diffusion of Li ion and suppress dendrite growth (Chen et al., 2019b). Pulse current could suppress dendrite growth via a kinetic-based molecular mechanism (Li et al., 2017). In another work, sinusoidal ripple current with a shelve time could lead to a charge relaxation and relieve the dendrite (Zhang et al., 2019). All of these approaches are based on the concept of preventing dendrite before its occurrence; in contrast, the route for repairing dendrite (a healing route) is rarely reported. Herein, we designed two types of route to suppress Li dendrite growth. One is intermittent-deposition route by a shelve time for charge relaxation mode (STCRM), corresponding to a common suppressing route. Another is asymmetrical-deposition route by reverse current for dendrite dissolution, named as asymmetrical bidirectional current mode (ABCM), of which the shelve time is changed into an anti-direction current, to dissolve the fresh-growth Li dendrite. By this strategy, Li dendrite can be suppressed with a synchronous healing mechanism (Figures 1 and S1). Commonly, Li dendrite will be aggravated under the continuous constant current, whereas during STCRM process, an inhomogeneous distribution of Li ion is changed into homogenization along with a charge relaxation,

[1]State Key Laboratory of Chem/Bio-Sensing and Chemometrics, Provincial Hunan Key Laboratory for Graphene Materials and Devices, College of Chemistry and Chemical Engineering, Hunan University, Changsha 410082, P. R. China

[2]These authors contributed equally

[3]Lead Contact

*Correspondence: wuyingpeng@hnu.edu.cn

https://doi.org/10.1016/j.isci.2019.100781

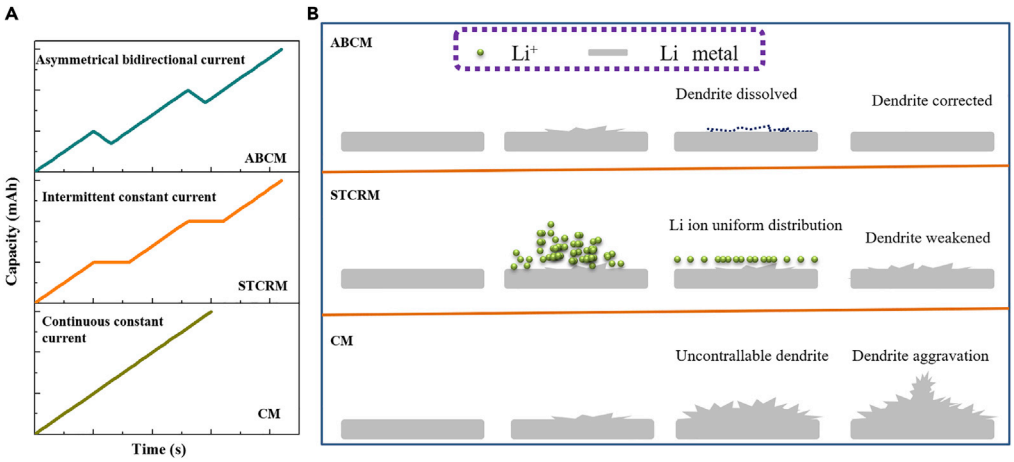


**Figure 1. The Schematic Diagram of Three Charging Modes of Li Metal Plating**

(A) The profiles of the applied current of three charging modes at the same special capacity and current density.

(B) A schematic diagram of CM (chronoamperometry mode), STCRM, and ABCM effecting on the growth/suppression of Li dendrite.

This figure is related to Table S1 and Figure S1.

resulting in a weakened dendrite. Although small-current-density way also can suppress the growth of Li dendrite, giving up the rate performance is incompatible (Zhang et al., 2016). In addition, small-current-density strategy will still meet the battery failure because of the continuously accumulated dendrite. A step further to perfection, using ABCM process, the new and mild dendrite can be corrected during anti-direction current. Then Li metal anode can be healed continually by a positive feedback mechanism.

## RESULT AND DISCUSSION

To prove this concept, first, an *in situ* electrochemical visual battery was taken to investigate the healing phenomena during mild dendrite state (detailed in Supplemental Information, Transparent Methods part), as shown in Figures 2, S2, and S3 and Videos S1, S2, S3, S4, S5, and S6 (Pang et al., 2017; Wood et al., 2016). Two types of dendrites (serious dendrites and weaken dendrites) can be found after their growth at 5 mA $cm^{-2}$. Figure 2A, S3A, and S3F and Videos S1 and S5 show that the large dendrite cannot be dissolved during the discharge state. On the contrary, Figures 2B, S3B, and S3G and Videos S2 and S6 show fresh and mild Li dendrite can be dissolved by anti-direction current. In addition, long-time Li plating behaviors at conditions of CM (chronoamperometry mode) and ABCM have been vividly exhibited (Figures 2C–2F and S3C–S3E and Videos S3 and S4). Under the condition of CM, the surface morphology is running to disorder and rough with a lot of dendrites (Figure 2C and Video S3). Oppositely, the surface morphology is kept smooth with micron-level Li sphere stacking closely by ABCM (Figure 2D and Video S4). Even at a special capacity of 3 mAh $cm^{-2}$, the surface of the ABCM sample is still smooth (Figure 2E), whereas dendrites are very serious and chaotically distributed for CM sample (Figures 2F and S3C–S3E). Commonly, vertical columnar dendrite would be easily corrected as mild dendrite, whereas branch dendrite would be difficult to be repaired as serious dendrite (Figure S3H and detailed in Supplemental Information). Noting that we use visual batteries only to prove our healing mechanism, the real batteries such as coin batteries and pouch cells are different from this type of battery (pressure, the mount of electrolyte, separator, and so on), and the data and discussion based on coin cell are shown in the following part. Moreover, to obtain a more intuitive experimental phenomenon to prove our concept, we have discussed different current density for lithium deposition and dissolution. Meanwhile, small dendrites can easily be corrected by tuning current density, which is proved by both modeling work and experiment (Yang et al., 2019). Additionally, it has been reported that 100% Li DoD (Depth of Discharge) in Li/S battery can lead to a better surface morphology than 36%, indicating that a reasonable surface can benefit the cyclic performance (100% discharge state means a smooth current collector, such as copper foil) (Mikhaylik et al., 2010). Therefore, healable Li metal anode can be obtained logically by corrected Li dendrite timely (holding a smooth surface always) using anti-direction current.

Figures S4A–S4F show polarizations of three type charge modes at pre-deposition Li/Li symmetrical cell system for 100 cycles (Li/Cu cell initially). All of them exhibit ~19 mV polarization at initial state. The

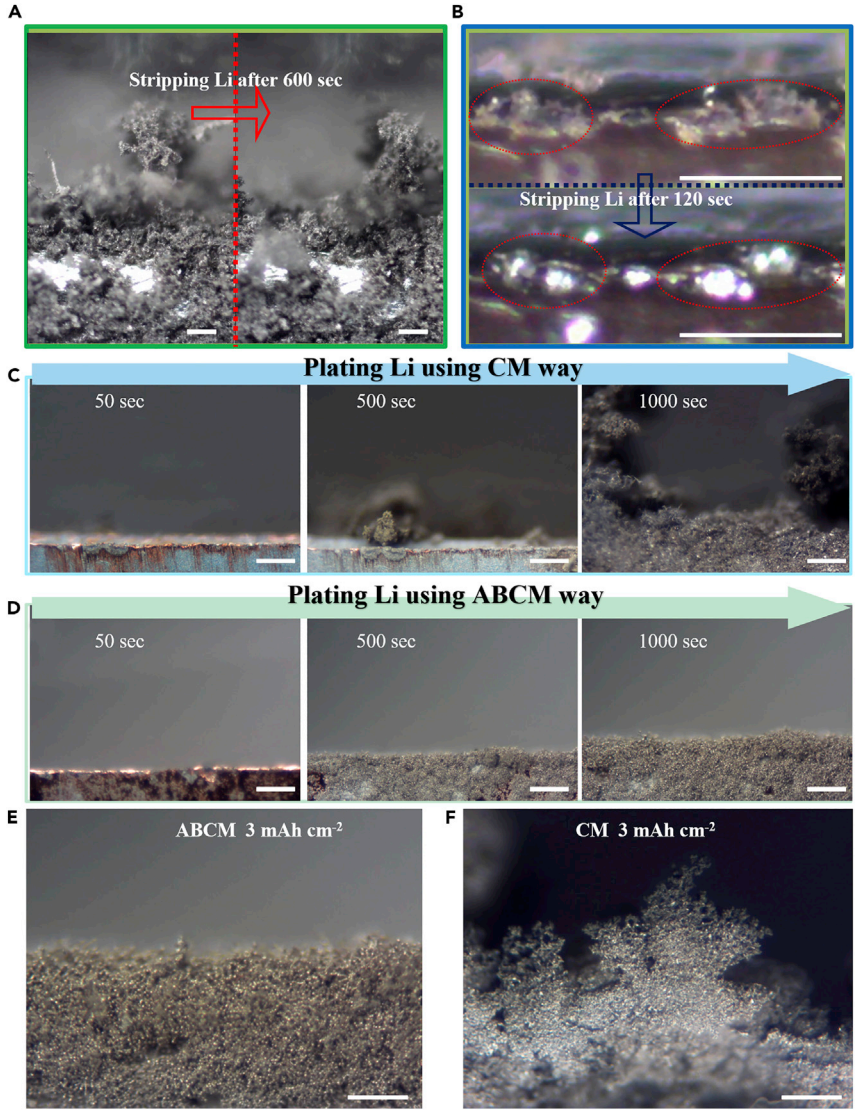


**Figure 2. *In Situ* Electrochemical Visual Battery for Tracking the Dendrite Dissolution**

(A) Serious dendrites-related irreparable surface state using Li/Li system.

(B) Mild and fresh dendrites-related repairable surface and dendrite-correcting course using Li/Li system.

(C) Plating Li by CM using Li/Cu system (5 mA $cm^{-2}$).

(D) Plating Li by ABCM using Li/Cu system (plating Li for 31 s and 5 mA $cm^{-2}$, dissolving dendrite for 5 s and 1 mA $cm^{-2}$).

(E) Plating Li by ABCM at 3 mAh $cm^{-2}$ using Li/Cu system (plating Li for 31 s and 5 mA $cm^{-2}$, dissolving dendrite for 5 s and 1 mA $cm^{-2}$).

(F) Plating Li by CM at 3 mAh $cm^{-2}$ using Li/Cu system (5 mA $cm^{-2}$).

The scale bar is 100 μm. This figure is related to Videos S1, S2, S3, and S4 and Figures S2 and S3.

electrochemical performance of CM sample became worse suddenly at 180 h (Figures S4A and B), and the polarization reached around 25 mV at the 100$^{th}$ cycle. On the contrary, Figures S4C–S4F indicate that STCRM and ABCM can keep a low and stable polarization around 15 mV. Magnified voltage profile at the 100$^{th}$ cycle demonstrates that CM leads a concave curve and the highest polarization (Figure S4B). Meanwhile, STCRM shows a pulse-shape voltage profile and a stable polarization, where the voltage in shelve-time of every charge/discharge step is above/below zero in order, correspondingly. In contrast, during charge/discharge progress of ABCM, every inverse voltage for correcting dendrite is below/above zero, respectively (Figure S4F). As intermittent current and bidirectional current modes cost more time under the same current density/cyclic capacity (Figures S4B, S4D, and S4F), herein, we also investigate these

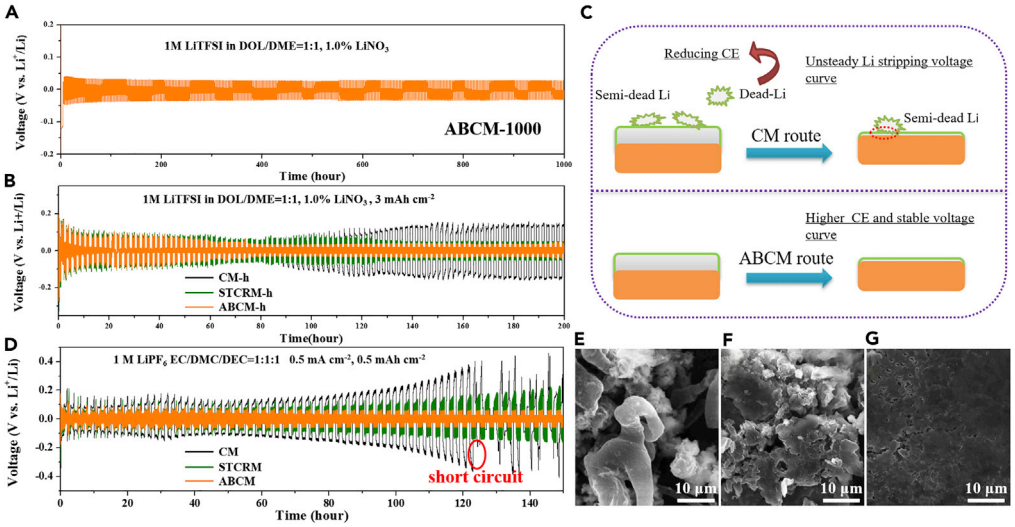


**Figure 3. The Polarization, Surface Morphology and Mechanism of Li Plating/Stripping by These Three Charging Modes**

(A) The 1,000-h polarization of ABCM (B2 in Table S1).

(B) The 200-h polarization of CM-h/STCRM-h/ABCM-h (as black, green, and orange curves; C6, C8, and C9 in Table S1, respectively) at the same cyclic time and capacity (3 mAh $cm^{-2}$) by using ether-based electrolyte.

(C) A schematic diagram of Coulombic Efficiency for CM and ABCM and a mechanism of semi-dead Li.

(D) The 150-h polarization of CM/STCRM/ABCM at the same current density (0.5 mA $cm^{-2}$) and capacity (0.5 mAh $cm^{-2}$) by using carbonate-based electrolyte.

(E) SEM of CM after 150-h symmetric cycling.

(F) SEM of STCRM after 150-h symmetric cycling.

(G) SEM of ABCM after 150-h symmetric cycling.

See E1–E3 in Table S1, correspondingly. This figure is related to Figures S8 and S10 and Table S1.

modes under the condition of same time and same cycle capacity, noting that ABCM and STCRM own different rates at the same current density and the same cyclic capacity (caused by anti-current time and shelved time, which cost more time, as shown in Figure 1A) from CM. To give a fair comparison, we take the same rate to evaluate these three modes in Figures S5–S7. All of the three modes have the same cyclic capacity at the same charge/discharge time. Under such conditions, STCRM and ABCM need a higher current density than CM at the normal charging and discharging process, as shown in Figure S1B. And the results show that, in spite of enlarging current density, STCRM and ABCM also exhibit better performance and more smooth deposited morphology.

In addition, in the view of initial nucleation affection, Li/carbon coating copper batteries were also investigated (detailed in Supplemental Information, Transparent Methods part) (Figures 3A and S8) (Chen et al., 2019a; Liu et al., 2019b; Lu et al., 2017; Pei et al., 2017). At the same pre-deposited condition, both STCRM and ABCM can keep long stable polarization for more than 1,000 h Figures 3A and S8 show both can tailor initial polarization mildly, and after only 40 cycles, the polarization reduced below 30 mV. As experiments went on, the polarization of STCRM only lasted about 600 h below 30 mV and then presented a significant increase. It is noteworthy that ABCM can hold the polarization around 27 mV for over 1,000 h. To give a more obvious comparison, Figure S8 gives voltage profiles of $200^{th}$, $600^{th}$, and $1{,}000^{th}$ h for STCRM and ABCM; it shows ABCM owns an obvious advantage for long cycles (37 mV [STCRM] versus 28 mV [ABCM] of the cycle at $1{,}000^{th}$ h). It suggests that optimized Li ion distribution and timely corrected surface state can successfully obtain a stable reduced polarization, which reflected in suppressing dendrite (Liu et al., 2018; Salvatierra et al., 2018). Especially, the ABCM route can lead to a more stable performance compared with the weakened dendrite mechanism, because the weakened dendrite mechanism will reach the critical failure point while aggregating lots of little dendrite within the long-term cycle. Furthermore, Figure S9 shows the sample at the ABCM condition of A3 in Table S1 also owns optimized performance, lasting for more than 800 h.

Additionally, we also investigated the polarization of these three modes for Li/Li cells (commercial lithium foil) at the same and 3-fold currents (see C1–C6 and C8–C9 in Table S1). Figure 3B shows the comparison at the same rate, and there is an obvious healing caused depolarization phenomenon during the early stage

of STCRM and ABCM, and the stable polarization below 50 mV could last more than 200 h. Although CM-h (refer to C6 in Table S1) owns the lowest initial polarization resulting from the lowest initial current density (CM [10 mV], STCRM [20 mV], and ABCM [18 mV], as shown in Figure S10), CM-h reveals an increasing polarization suddenly and continuously, which is affected by the nucleation and surface electron distribution. After 90-h loops, CM-h presents the highest polarization in these three samples. Meanwhile, the STCRM-h (refer to C8 in Table S1) exhibits a stable and tailoring polarization and the polarization is around 60 mV. In contrast, ABCM-h (refer to C9 in Table S1) shows the best cyclic performance, where a tailoring polarization becomes smaller and smaller gradually and stable at 35 mV. Moreover, Figure S11 illustrates ABCM also owns obvious advantage than CM and STCRM at 1 mAh $cm^{-2}$. Based on those electrochemical results, it is clear that the STCRM and ABCM surpass the traditional CM in the aspect of stability, duration, and smaller polarization, whereas ABCM offers the lowest polarization and the best stability. Generally, all of symmetrical cell systems (Li foil/Li foil or deposited Li/Li foil) show ABCM can always obtain the most stable polarization.

In addition, in carbonate-based electrolyte, CM exhibits a continuous increasing polarization and a sudden reducing at 120 h (short circuit); STCRM likewise shows a continuous increasing polarization, but the polarization is still smaller than CM. Meanwhile, ABCM owns the lowest and most stable polarization of ~60 mV (Figure 3D). For the pre-deposited Li metal (13 mAh $cm^{-2}$), CM cannot last more than 75 h at 1 mA $cm^{-2}$ and 1 mAh $cm^{-2}$, in contrast with the stable cycle performance of ABCM (Figure S12). In general, ABCM exhibits the best performances not only in ether-based electrolyte but also in carbonate-based electrolyte.

Figure S13 gives voltage-time curves of Li/Cu cell for CM and ABCM; each cell was deposited with the same amount of Li on carbon-coated copper, then after 10 loops of CM or ABCM route (the same as A1 or A3, respectively), the Li on carbon-coated copper is striped by electrochemical dissolution under 2V, then C.E. (Coulombic Efficiency) can be calculated and labeled on the corresponding cycle (Adams et al., 2018; Fan et al., 2018). The C.E. of CM sample is lower than that of ABCM, the C.E.s of five loops for CM are 96.3%, 97.6%, 77.2%, 95.1%, and 90.0% in order. Correspondingly, C.E.s of five loops for ABCM are 95.2%, 97.2%, 98.0%, 97.6%, and 94.4%, respectively (Figure S13). Hypothetically, pre-deposited Li metal owns 100% C.E., thereof, for 50 cycles of these three modes, the average C.E.s of CM/STCRM/ABCM can be gained as 91.24/95.60/96.28%, respectively (Figures S13 and S14). It means both STCRM and ABCM exhibit optimized reversible reaction and ABCM owns the best reversibility. Meanwhile, Figure S13B demonstrates that, during the final striping course, the voltage curve of CM is disorder and churning. On the contrary, ABCM leads to a more stable process (Figure S13D). Possibly, CM has more side reaction or more dead Li/semi-dead Li. The dead Li is electrically isolated from the substrate and semi-dead Li means that Li metal contacts with Li metal by some shared SEI film (Figure 3C); meanwhile a recent report has proved semi-dead Li real existed (Fang et al., 2019). The bulk Li source on substrate can be stripped smoothly; however, the semi-dead Li induces more electronic resistance due to the shared SEI film. Along with increasing stripping voltage, the resistance of shared SEI film may be breakdown, resulting in an inauthentic C.E. data (Figure S13B). Besides, carbonate-based electrolyte has also been investigated for C.E., indicating that ABCM exhibits better performance than CM (Figure S15). Although ABCM can optimize C.E. performance in these two types of electrolyte, the intrinsic SEI is still a dominant issue for the protection and effective utilization of lithium metal anode.

Correspondingly, Figures 3E–3G, 4A–4G, and S16A–S16E give the morphology, chemical component of SEI film, and interfacial impedance. In the carbonate-based electrolyte, scanning electron microscopy (SEM) shows that ABCM exhibits a dendrite-free surface, in contrast with accumulation of Li pieces (STCRM) and serious dendrites (CM) (Figures 3E–3G). Besides we also investigate the surface morphology in ether-based electrolyte. Obviously, the morphology of the CM sample is rough and chaotic (Figures 4A and S16A). Figures 4B, 4C, S16B, and S16C illustrate a flat surface and the Li anode is assembled via a uniform zoned distribution, and the zoned areas of STCRM-100 and ABCM-100 are around 40 and 200 $\mu m^2$ (the average particle size distribution is 6.4 $\mu$m [STCRM-100] and 13 $\mu$m [ABCM-100], as shown in Figures S18A and S18B), respectively. Figures 4D and S16D present the surface morphology of STCRM after 1,000-h cycles. Although the polarization in STCRM is a little worse (Figure S8A), the surface morphology exhibits obvious roughness and pulverization (Figures 4D and S16D). At the same time, ABCM (Figures 4E and S16E) still exhibits a free-dendrite surface morphology, indicating the healable Li metal anode using corrected dendrite mechanism is more advanced and practical than a weakened dendrite mechanism (STCRM) during long-term cycles, and this result highly proves our concept (Figure 1B). Furthermore,

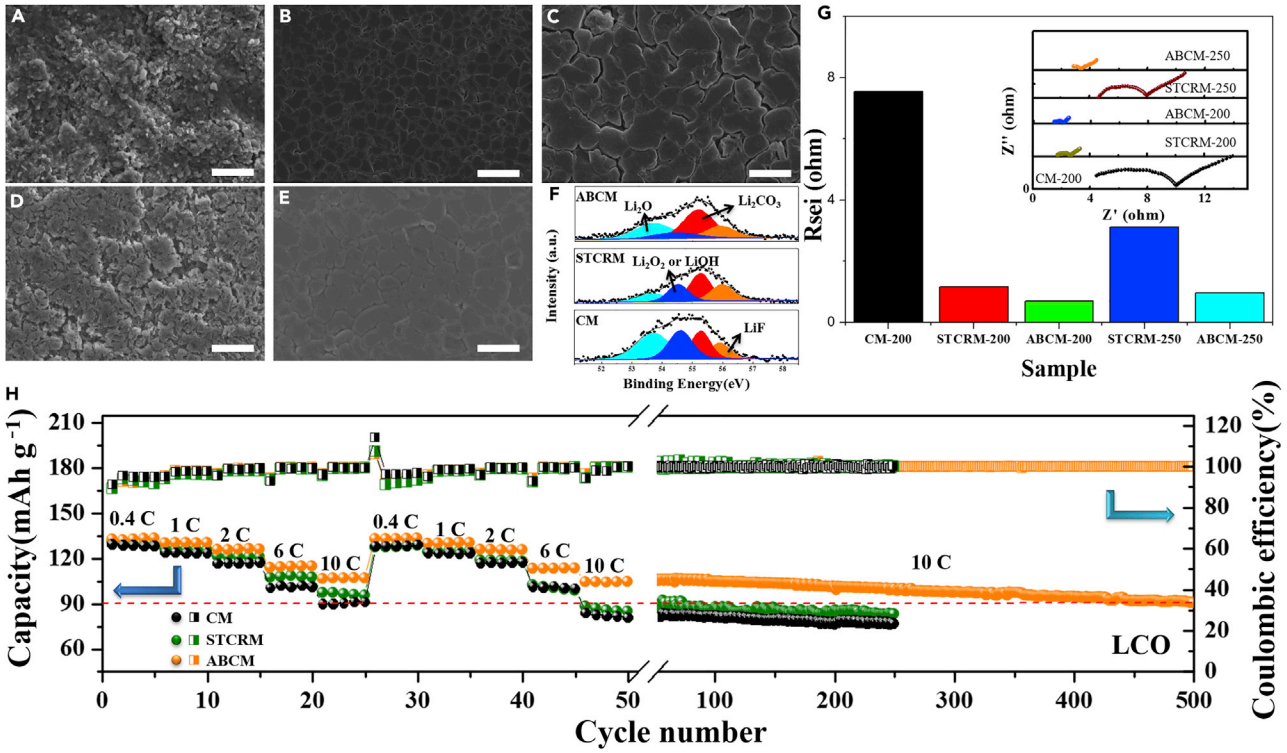


**Figure 4. Surface Morphology and Impedance of Cyclic Li Metal Battery via These Three Type Modes**

(A–E) are SEM of CM-100, STCRM-100, ABCM-100, STCRM-1000, and ABCM-1000, respectively.

(F) Peak fitting of Li 1 s after Ar ion etch for ABCM, STCRM, and CM.

(G) The calculated SEI-film impedances of these EIS data. The illustration in Figure 4G shows the impedances of three samples, CM-200, STCRM-200, and ABCM-200, mean cycling for 200 cycles, and STCRM-250 and ABCM-250 mean going on cycling to 250 cycles (3 mA/cm$^{-2}$). See A10–A12 in Table S1.

(H) Rate capacity and long-term stability of CM, STCRM, and ABCM at 0.4 C, 1 C, 2 C, 6 C, 10 C (at the rate stage) and 10 C (at the long cycle stage) for Li/$LiCoO_2$ batteries. (The full circle stands for the specific discharge capacity, and the half-filled squares are the Coulombic Efficiency).

The scale bars in (A–E) are 20 μm. This figure is related to Figures S4, S16, S18, S19, and S22 and Table S1.

X-ray photoelectron spectroscopy (XPS) was taken to analyze the differences between the three modes with carbonate-based electrolyte. We focus on F element, for it is stable to air and can reveal the information of the top-layer SEI. Herein, F1s fitting data are shown in Figures S17A–S17C: CM owns the obvious highest concentration of LiF peak (at ~685.1 eV, 44.8%) in contrast with ABCM (25.1%) and STCRM (43.2%) (Liu et al., 2019c). As we know, the surface of SEI film is mainly constructed by organic fragment. The more the Li dendrite, the more the consumption of electrolyte and the more the formation of SEI, therefore, leading to a high concentration of LiF. Based on this, the XPS data can tell that the ABCM produces the fewest dendrites. After Ar ion etching (~16 nm deep), information of the bottom SEI film has been investigated. The organic layer has been eliminated completely, because the peaks of organic component in F1s C1s O1s are not observed (Figures S17D–S17H) (Eshkenazi et al., 2004; Wang et al., 2018b). Therefore, Li 1s peak fitting data in Figure 4F give the real information of the inorganic layer, which is near the Li metal. The peak at ~54.5 eV stems from $Li_2O_2$ and LiOH, which is an unstable state (Lu et al., 2008; Nasybulin et al., 2013). By contrast, the peaks at around 53.7, 55.1, and 55.9 eV are originated from $Li_2O$, $Li_2CO_3$, and LiF, respectively (Edström et al., 2006; Liu et al., 2019a). Obviously, the peak at ~54.5 eV in ABCM is the weakest, indicating the fewest broken SEI in ABCM route, which can be attributed to that very few new Li metal (dendrite) contacted with electrolyte by this route. The surface of ABCM-1000 (refer to B2 in Table S1) is still maintained at an average particle size of ~10 μm (Figure S18C), in contrast with a disorder surface morphology of STCRM-1000 (refer to B1 in Table S1). Generally, there is rare dendrite by ABCM route, which is not serious for the battery system; by contrast, lots of dendrites and dead Li/semi-dead Li make battery deteriorative by the CM route (Chen et al., 2017).

Figure 4G gives electrochemical impedance spectra (EIS) of these routes using higher rate performance (A10–12 as shown in Table S1); the arc curve in the illustration means the impedance of SEI film (Bieker

et al., 2015). Therefore, CM-200 (refer to A10 in Table S1) exhibits the highest interface impedance. Simultaneously, ABCM-200/250 (refer to A12 in Table S1) exhibits excellent impedance at about 0.69 and 0.96 ohm, respectively. In addition, side reaction and dendrite would increase the interface impedance from electrolyte and electrode inherent character, named Rs (Figure S19) (Wang et al., 2018a). Obviously, CM-200 and STCRM-200/250 (refer to A11 in Table S1) exhibit higher Rs than ABCM 200/250. Figures S20 and S21 also give EIS data corresponding to Figures 4A–4E, where ABCM exhibits absolute advantage in long-term cycle and some advantage in short cycle, in accordance with the conclusion that traditional route (STCRM) can stabilize the Li metal anode via weakening dendrite; however, battery of STCRM will fail when dendrites accumulate too much. All of these results illustrate the ABCM route can provide a stable and long-life Li metal anode. These EIS data indicate ABCM can effectively heal dendrites without more electrolyte consumption (low Rs) and thicker SEI film (Low Rsei). Obviously, ABCM in ether electrolyte can get better performance than in carbonate-based electrolyte. Thereof, this technology is an optimized route and can reach stable Li metal anode with adaptive SEI film, showing a promise to reach the real practical application. Furthermore, full cells (Li/LCO battery) are taken to investigate the rate and duration of these three modes (Figures 4H, S22A, and S22B). By contrast, ABCM demonstrates the best performance at all current densities from 0.4 to 10 C and CM exhibits the worst performance. After 50 loops, the ABCM sample continues to cycle up to 500 cycles at 10 C and still exhibits ~90 mAh $g^{-1}$ capacity. The 500 cycles performances of CM, STCRM, and ABCM at 10 C are also shown in Figure S22. Although the average C.E.s are similar (~99.7%), ABCM has the smallest fluctuation and exhibits the highest capacity retention as 83.9%, in contrast to 79.9% and 66.2% for STCRM and CM, respectively.

Moreover, Figure S23 shows that different Li plating time can affect the polarization, and Figure S24 shows that different dendrite correcting time can also directly affect the polarization. Therefore, we also should consider that irreparable surface can highly dominate the cyclic performance (Figure 1B). Meanwhile, different plating/dissolving times can induce different states (Figure S25): for ABCM-a, the dendrite cannot be repaired under the condition of C7 in Table S1, which results in sustained increasing polarization; however, for ABCM-b, under the condition of C9 in Table S1, the dendrite can be repaired and results in a healable polarization. Therefore, correcting dendrites timely is necessary in the ABCM process, which further proves our view of correcting dendrite.

### Conclusion

Herein a healing route for suppressing Li dendrite was investigated, which corrects mild dendrite timely via reverse current. This route can effectively suppress Li dendrite, in contrast with traditional suppressing route, e.g., STCRM. ABCM exhibits a more promising way to obtain stable and long-life Li anode, because of eliminating Li dendrite timely and avoiding the positive feedback cycle, avoiding the agminated small dendrites reaching a critical failure point of battery by STCRM. In general, different from conventional suppressing Li dendrite, e.g., SEI film, nucleation route, and so on, our route puts forward another way (corrected dendrite timely for healing) to suppress dendrite. Our work indicates the improved charge protocol is also important for stable Li metal battery (different charge protocol is widely used in Li ion battery for increasing rate performance) (Alcaraz et al., 2017). And, the idea of correcting dendrite before the irreparable deterioration is proved as a promising way to harvest stable and dendrite-free Li metal anode. This viewpoint can be extended to other alkali metal electrodes, such as Na, K, and Zn.

### Limitations of the Study

Our charging technique contains an anti-direction current for a short time regularly during charge, which causes a small energy loss of the battery. This loss of energy is quite little but should not be neglected (less than 15% in our work). Such energy loss is a secondary issue in contrast to the safety of the Li metal anode; however, efforts are still needed to minimize this energy loss in the further work.

## METHODS

All methods can be found in the accompanying Transparent Methods supplemental file.

## SUPPLEMENTAL INFORMATION

Supplemental Information can be found online at https://doi.org/10.1016/j.isci.2019.100781.

## ACKNOWLEDGMENTS

Y.W. acknowledges financial support from the Fundamental Research Funds for the Central Universities (531107051077), National Natural Science Foundation of China (Grant No. 21805079), and Hunan high-level talent gathering project (2018RS3054); D.W. acknowledges financial support from the Fundamental Research Funds for the Central Universities (531107051230); L.H. acknowledges financial support from the Fundamental Research Funds for the Central Universities (531107051042), National Natural Science Foundation of China (Grant No. 21805078).

## AUTHOR CONTRIBUTIONS

Y.W. and D.W. conceived the idea and designed the experiments. D.W. and C.Q. performed most of the experiments. Y.W., D.W., and C.Q. analyzed the main data. X.L., G.S., Y.L., M.C., and L.H. participated in the experiments for sample preparation, characterization, and data collection. D.W., Y.W., and C.Q. drafted the manuscript. All authors participated in the interpretation of the data and production of the final manuscript.

## DECLARATION OF INTERESTS

The authors declare no competing interests.

Received: August 4, 2019
Revised: November 10, 2019
Accepted: December 12, 2019
Published: January 24, 2020

## REFERENCES

Adams, B.D., Zheng, J., Ren, X., Xu, W., and Zhang, J.-G. (2018). Accurate determination of coulombic efficiency for lithium metal anodes and lithium metal batteries. Adv. Energy Mater. *8*, 1702097.

Alcaraz, C., Lopez, J., and Wolthusen, S. (2017). OCPP protocol: security threats and challenges. IEEE T. Smart Grid *8*, 2452–2459.

Bieker, G., Winter, M., and Bieker, P. (2015). Electrochemical in situ investigations of SEI and dendrite formation on the lithium metal anode. Phys. Chem. Chem. Phys. *17*, 8670–8679.

Chen, K.-H., Wood, K.N., Kazyak, E., LePage, W.S., Davis, A.L., Sanchez, A.J., and Dasgupta, N.P. (2017). Dead lithium: mass transport effects on voltage, capacity, and failure of lithium metal anodes. J. Mater. Chem. A *5*, 11671–11681.

Chen, X., Chen, X.-R., Hou, T.-Z., Li, B.-Q., Cheng, X.-B., Zhang, R., and Zhang, Q. (2019a). Lithiophilicity chemistry of heteroatom-doped carbon to guide uniform lithium nucleation in lithium metal anodes. Sci. Adv. *5*, eaau7728.

Chen, Y., Dou, X., Wang, K., and Han, Y. (2019b). Lithium dendrites inhibition via diffusion enhancement. Adv. Energy Mater. *9*, 1900019.

Cheng, X.-B., Zhang, R., Zhao, C.-Z., and Zhang, Q. (2017). Toward safe lithium metal anode in rechargeable batteries: a review. Chem. Rev. *117*, 10403–10473.

Deng, Y.-P., Wu, Z.-G., Liang, R., Jiang, Y., Luo, D., Yu, A., and Chen, Z. (2019). Layer-based heterostructured cathodes for lithium-ion and sodium-ion batteries. Adv. Funct. Mater. *29*, 1808522.

Ding, F., Xu, W., Graff, G.L., Zhang, J., Sushko, M.L., Chen, X., Shao, Y., Engelhard, M.H., Nie, Z., Xiao, J., et al. (2013). Dendrite-free lithium deposition via self-healing electrostatic shield mechanism. J. Am. Chem. Soc. *135*, 4450–4456.

Edström, K., Herstedt, M., and Abraham, D.P. (2006). A new look at the solid electrolyte interphase on graphite anodes in Li-ion batteries. J. Power Sources *153*, 380–384.

Eshkenazi, V., Peled, E., Burstein, L., and Golodnitsky, D. (2004). XPS analysis of the SEI formed on carbonaceous materials. Solid State Ionics *170*, 83–91.

Fan, X., Chen, L., Ji, X., Deng, T., Hou, S., Chen, J., Zheng, J., Wang, F., Jiang, J., Xu, K., et al. (2018). Highly fluorinated interphases enable high-voltage Li-metal batteries. Chem *4*, 174–185.

Fang, C., Li, J., Zhang, M., Zhang, Y., Yang, F., Lee, J.Z., Lee, M.-H., Alvarado, J., Schroeder, M.A., Yang, Y., et al. (2019). Quantifying inactive lithium in lithium metal batteries. Nature *572*, 511–515.

Hou, G., Sun, Q., Ai, Q., Ren, X., Xu, X., Guo, H., Guo, S., Zhang, L., Feng, J., Ding, F., et al. (2019). Growth direction control of lithium dendrites in a heterogeneous lithiophilic host for ultra-safe lithium metal batteries. J. Power Sources *416*, 141–147.

Huang, Y., Liu, J., Wang, J., Hu, M., Mo, F., Liang, G., and Zhi, C. (2018). An intrinsically self-healing NiCo||Zn rechargeable battery with a self-healable ferric-ion-crosslinking sodium polyacrylate hydrogel electrolyte. Angew. Chem. Int. Ed. *57*, 9810–9813.

Hundekar, P., Basu, S., Pan, J., Bartolucci, S.F., Narayanan, S., Yang, Z., and Koratkar, N. (2019). Exploiting self-heat in a lithium metal battery for dendrite healing. Energy Storage Mater. *20*, 291–298.

Li, Q., Tan, S., Li, L., Lu, Y., and He, Y. (2017). Understanding the molecular mechanism of pulse current charging for stable lithium-metal batteries. Sci. Adv. *3*, e1701246.

Li, L., Basu, S., Wang, Y., Chen, Z., Hundekar, P., Wang, B., Shi, J., Shi, Y., Narayanan, S., and Koratkar, N. (2018a). Self-heating–induced healing of lithium dendrites. Science *359*, 1513–1516.

Li, Q., Pan, H., Li, W., Wang, Y., Wang, J., Zheng, J., Yu, X., Li, H., and Chen, L. (2018b). Homogeneous interface conductivity for lithium dendrite-free anode. ACS Energy Lett. *3*, 2259–2266.

Liang, X., Pang, Q., Kochetkov, I.R., Sempere, M.S., Huang, H., Sun, X., and Nazar, L.F. (2017). A facile surface chemistry route to a stabilized lithium metal anode. Nat. Energy *2*, 17119.

Liang, Z., Yan, K., Zhou, G., Pei, A., Zhao, J., Sun, Y., Xie, J., Li, Y., Shi, F., Liu, Y., et al. (2019). Composite lithium electrode with mesoscale skeleton via simple mechanical deformation. Sci. Adv. *5*, eaau5655.

Lin, D., Liu, Y., and Cui, Y. (2017). Reviving the lithium metal anode for high-energy batteries. Nat. Nanotechnol. *12*, 194–206.

Liu, S., Wang, A., Li, Q., Wu, J., Chiou, K., Huang, J., and Luo, J. (2018). Crumpled graphene balls stabilized dendrite-free lithium metal anodes. Joule *2*, 184–193.

Liu, Q., Liu, Y., Jiao, X., Song, Z., Sadd, M., Xu, X., Matic, A., Xiong, S., and Song, J. (2019a).

Enhanced ionic conductivity and interface stability of hybrid solid-state polymer electrolyte for rechargeable lithium metal batteries. Energy Storage Mater. *23*, 105–111.

Liu, W., Xia, Y., Wang, W., Wang, Y., Jin, J., Chen, Y., Paek, E., and Mitlin, D. (2019b). Pristine or highly defective? Understanding the role of graphene structure for stable lithium metal plating. Adv. Energy Mater. *9*, 1802918.

Liu, X., Wang, D., Yang, X., Zhao, Z., Yang, H., Feng, M., Zhang, W., and Zheng, W. (2019c). Synergistic dual-confinement effect: merit of hollowly metallic Co9S8 in packaging enhancement of electrochemical performance of Li–S batteries. ACS Appl. Energy Mater. *2*, 1428–1435.

Lu, M., Cheng, H., and Yang, Y. (2008). A comparison of solid electrolyte interphase (SEI) on the artificial graphite anode of the aged and cycled commercial lithium ion cells. Electrochim. Acta *53*, 3539–3546.

Lu, Y., Tu, Z., and Archer, L.A. (2014). Stable lithium electrodeposition in liquid and nanoporous solid electrolytes. Nat. Mater. *13*, 961.

Lu, L.-L., Zhang, Y., Pan, Z., Yao, H.-B., Zhou, F., and Yu, S.-H. (2017). Lithiophilic Cu–Ni core–shell nanowire network as a stable host for improving lithium anode performance. Energy Storage Mater. *9*, 31–38.

Mikhaylik, Y.V., Kovalev, I., Schock, R., Kumaresan, K., Xu, J., and Affinito, J. (2010). High energy rechargeable Li-S cells for EV application: status, remaining problems and solutions. ECS Trans. *25*, 23–34.

Nasybulin, E., Xu, W., Engelhard, M.H., Nie, Z., Burton, S.D., Cosimbescu, L., Gross, M.E., and Zhang, J.-G. (2013). Effects of electrolyte salts on the performance of Li–O2 batteries. J. Phys. Chem. C *117*, 2635–2645.

Pang, Q., Liang, X., Shyamsunder, A., and Nazar, L.F. (2017). An in vivo formed solid electrolyte surface layer enables stable plating of Li metal. Joule *1*, 871–886.

Pei, A., Zheng, G., Shi, F., Li, Y., and Cui, Y. (2017). Nanoscale nucleation and growth of electrodeposited lithium metal. Nano Lett. *17*, 1132–1139.

Qiao, Y., Yi, J., Wu, S., Liu, Y., Yang, S., He, P., and Zhou, H. (2017). Li-CO 2 electrochemistry: a new strategy for CO 2 fixation and energy storage. Joule *1*, 359–370.

Salvatierra, R.V., López-Silva, G.A., Jalilov, A.S., Yoon, J., Wu, G., Tsai, A.-L., and Tour, J.M. (2018). Suppressing Li metal dendrites through a solid Li-ion backup layer. Adv. Mater. *30*, 1803869.

Shen, K., Wang, Z., Bi, X., Ying, Y., Zhang, D., Jin, C., Hou, G., Cao, H., Wu, L., Zheng, G., et al. (2019). Magnetic field–suppressed lithium dendrite growth for stable lithium-metal batteries. Adv. Energy Mater. *9*, 1900260.

Shi, P., Zhang, L., Xiang, H., Liang, X., Sun, Y., and Xu, W. (2018). Lithium difluorophosphate as a dendrite-suppressing additive for lithium metal batteries. ACS Appl. Mater. Interfaces *10*, 22201–22209.

Wang, D., Zhang, W., Zheng, W., Cui, X., Rojo, T., and Zhang, Q. (2017a). Towards high-safe lithium metal anodes: suppressing lithium dendrites via tuning surface energy. Adv. Sci. *4*, 1600168.

Wang, L., Zhang, L., Wang, Q., Li, W., Wu, B., Jia, W., Wang, Y., Li, J., and Li, H. (2017b). Long lifespan lithium metal anodes enabled by Al2O3 sputter coating. Energy Storage Mater. *10*, 16–23.

Wang, D., Luan, C., Zhang, W., Liu, X., Sun, L., Liang, Q., Qin, T., Zhao, Z., Zhou, Y., Wang, P., et al. (2018a). Zipper-inspired SEI film for remarkably enhancing the stability of Li metal anode via nucleation barriers controlled weaving of lithium pits. Adv. Energy Mater. *8*, 1800650.

Wang, D., Zhang, W., Drewett, N.E., Liu, X., Yoo, S.J., Lee, S.-G., Kim, J.-G., Deng, T., Zhang, X., Shi, X., et al. (2018b). Exploiting anti-T-shaped graphene architecture to form low tortuosity, sieve-like interfaces for high-performance anodes for Li-based cells. ACS Cent. Sci. *4*, 81–88.

Wang, X., Zeng, W., Hong, L., Xu, W., Yang, H., Wang, F., Duan, H., Tang, M., and Jiang, H. (2018c). Stress-driven lithium dendrite growth mechanism and dendrite mitigation by electroplating on soft substrates. Nat. Energy *3*, 227–235.

Wang, A., Deng, Q., Deng, L., Guan, X., and Luo, J. (2019). Eliminating tip dendrite growth by Lorentz force for stable lithium metal anodes. Adv. Funct. Mater. *29*, 1902630.

Westover, A.S., Dudney, N.J., Sacci, R.L., and Kalnaus, S. (2019). Deposition and confinement of Li metal along an artificial lipon–lipon interface. ACS Energy Lett. *4*, 651–655.

Wood, K.N., Kazyak, E., Chadwick, A.F., Chen, K.-H., Zhang, J.-G., Thornton, K., and Dasgupta, N.P. (2016). Dendrites and pits: untangling the complex behavior of lithium metal anodes through operando Video microscopy. ACS Cent. Sci. *2*, 790–801.

Xu, Y., Li, T., Wang, L., and Kang, Y. (2019). Interlayered dendrite-free lithium plating for high-performance lithium-metal batteries. Adv. Mater. *31*, 1901662.

Yang, H., Fey, E.O., Trimm, B.D., Dimitrov, N., and Whittingham, M.S. (2014). Effects of Pulse Plating on lithium electrodeposition, morphology and cycling efficiency. J. Power Sources *272*, 900–908.

Yang, C.P., Yin, Y.X., Zhang, S.F., Li, N.W., and Guo, Y.G. (2015). Accommodating lithium into 3D current collectors with a submicron skeleton towards long-life lithium metal anodes. Nat. Commun. *6*, 8058.

Yang, Q., Liang, G., Guo, Y., Liu, Z., Yan, B., Wang, D., Huang, Z., Li, X., Fan, J., and Zhi, C. (2019). Do zinc dendrites exist in neutral zinc batteries: a developed electrohealing strategy to in situ rescue in-service batteries. Adv. Mater. *31*, 1903778.

Zhang, R., Cheng, X.-B., Zhao, C.-Z., Peng, H.-J., Shi, J.-L., Huang, J.-Q., Wang, J., Wei, F., and Zhang, Q. (2016). Conductive nanostructured scaffolds render low local current density to inhibit lithium dendrite growth. Adv. Mater. *28*, 2155–2162.

Zhang, R., Li, N.-W., Cheng, X.-B., Yin, Y.-X., Zhang, Q., and Guo, Y.-G. (2017). Advanced micro/nanostructures for lithium metal anodes. Adv. Sci. *4*, 1600445.

Zhang, H., Eshetu, G.G., Judez, X., Li, C., Rodriguez-Martínez, L.M., and Armand, M. (2018). Electrolyte additives for lithium metal anodes and rechargeable lithium metal batteries: progress and perspectives. Angew. Chem. Int. Ed. *57*, 15002–15027.

Zhang, Z., Wang, Z.L., and Lu, X. (2019). Suppressing lithium dendrite growth via sinusoidal ripple current produced by triboelectric nanogenerators. Adv. Energy Mater. *9*, 1900487.

Zhang, W., Wang, D., and Zheng, W. (2020). A semiconductor-electrochemistry model for design of high-rate Li ion battery. J. Energy Chem. *41*, 100–106.

Zhao, Y., Li, G., Gao, Y., Wang, D., Huang, Q., and Wang, D. (2019). Stable Li metal anode by a hybrid lithium polysulfidophosphate/polymer cross-linking film. ACS Energy Lett. *4*, 1271–1278.

Zhu, J., Wu, Y., Huang, X., Huang, L., Cao, M., Song, G., Guo, X., Sui, X., Ren, R., and Chen, J. (2019). Self-healing liquid metal nanoparticles encapsulated in hollow carbon fibers as a free-standing anode for lithium-ion batteries. Nano Energy *62*, 883–889.

**ISCI, Volume *23***

## Supplemental Information

# Synchronous Healing of Li Metal Anode via Asymmetrical Bidirectional Current

**Dong Wang, Chichu Qin, Xilong Li, Ganqiang Song, Yumin Liu, Mengyang Cao, Lu Huang, and Yingpeng Wu**

# Supplemental Information

## TRANSPARENT METHODS

### Materials

$LiCoO_2$, copper foil, carbon coated copper foil and Celgard 2325 were purchased from Shenzhen Kejing Star Technology Co., Ltd., China. All the electrolytes were purchased from Suzhou dodochem Ltd., China. Lithium foil were provided by China Energy Lithium Co., Ltd.. Copper foils were ultrasonic treated with acetone and ethanol (purchased from China National Medicines Co., Ltd.) for 5 min and subsequently with deionized water to remove surface impurities. All the other chemicals were used as received without further purification.

### Electrochemical measurements

CR2032 type coin cells were assembled in a glove box filled by Ar gas (>99.99%) within the $O_2$ and $H_2O$ less than 0.1 ppm. The separator is Celgard 2325 membrane. Three kinds of electrolyte are used: a ether based electrolyte (1M lithium bis(trifluoromethanesulfonyl)imide (LiTFSI) in 1, 3-dioxolane (DOL)/1, 2-dimethoxyethane (DME)=1:1, 1.0% $LiNO_3$) and a carbonate based electrolyte (1M $LiPF_6$ in EC/DMC/DEC=1:1:1) for symmetric battery system. MSK-110 is used for cell assembly. In order to study the effects of these routes on suppressing dendrite, we firstly investigated two different types of symmetric batteries. The first one is a lithium/current collector (Li/Cu; Li/carbon coated copper) batteries, forming pre-deposited Li/Li symmetric battery by pre-depositing a certain amount of lithium on copper or carbon-coated copper (a current density of 5 mA $cm^{-2}$ for Li nucleation for 12 min, and then a current density of 3 mA $cm^{-2}$ for further epitaxial growth of lithium metal on its surface for 4 h). Herein, copper foil (12 mm) or carbon coating copper foil (12 mm) and commercial lithium foil (16 mm) are assembled as the cathode and anode, respectively. The second one is a traditional lithium/lithium (commercial Li foil, 16 mm) system. Subsequently, we compared the electrochemical performance of full batteries (Commercial $LiCoO_2$ as cathode) with the three charging modes. Every coin battery uses about 0.1 mL electrolyte.

Three types of charge-discharge mode (CM STCRM and ABCM) were used for symmetric cycle, as shown in Figure 1a. Herein, different courses were applied to investigate the polarization and C.E. and the detailed processes were listed in table 1. All the charge-discharge tests were operated on a Neware battery testing system with constant temperature of 25±0.1 ˚C or room temperature.

Commonly, 50 μm thick Li metal owns about 10 mAh $cm^{-2}$, herein we use two types of Lithium metal anode with different capacities, one is commercial lithium foil (~400 μm, ~80 mAh $cm^{-2}$) and the other is pre-deposited Li metal anode (13 mAh $cm^{-2}$, ~65 μm). The transformation between thickness and capacity is calculated by 1 μm ≈ 5 mAh $cm^{-2}$(Liu et al., 2019).

### Electrochemical Impedance Spectroscopy

In order to study the interface impedance of these three modes, electrochemical impedance spectroscopy (EIS) was chosen to test electrolyte impedance and SEI film impedance in different cycle stages. All of EIS data was characterized in two-electrode mode by an electrochemical workstation (IVIUM-VERTEX. C, Netherlands) with the frequency range from 100000 Hz to 1 Hz, as well as the frequency points was 71 and the amplitude was 0.01 V.

**Dendrite observation by in situ electrochemical visual cell**

***The process of making electrode and electrolytic cell for in situ dendrite observation:***

In glove box**,** a electrolytic cell (751 cuvette: 7.5×12.5×45 mm, with a volume of 1.7 mL and a light path of 5 mm) was assembled, as shown in Fig. S2a. Firstly two copper sheets (0.25 mm thick) was cut into 0.25 mm thick, 37.4 mm long and beyond 3 mm wide, then wrapped with a thin wire. After that, we pressed the lithium foil into a copper sheet side. Li contained copper was used as a counter electrode and another copper sheet was acted as a working electrode, then all of these were encapsulated in the cuvette. A wire was taken out from the two homemade poles of the cuvette cap, parafilm was then used to seal the edge. Subsequently we injected the electrolyte (ether or carbonate based) from the small hole in the top of the cover with a syringe while controlling the height of the electrolyte to 30 mm. In the end, this hole also need sealed up to make sure no air can leak in. (In Li/Li systems, both of the two copper sheets were coated with lithium foil, the rest parts were the same as the above pre-deposited Li/Li system operations.)

***Simultaneous process of electrochemical measurement and dendrite observation：***

A microscope (Phenix PH50-1B43L-PL) was placed parallel and upside down on the laboratory table, with the prepared electrolytic cell vertically fixed on its stage, as shown in Fig. S2b. Then two wires from the electrolytic cell were connected to the testing system. Subsequently, the electronic eyepiece on the microscope was connected with computer. Two types of dendrite (serious dendrites and weaken dendrites) are formed and found at the current of about 5 mA $cm^{-2}$ by applied external electric field, soon a reverse current of 5 mA $cm^{-2}$ was applied to observe the dissolution behavior of dendrites.

**Electrodes Characterization:**

All sample morphologies presented in this experiment were characterized by scanning electron microscopy (SEM, KYKY-EM6200). The sealed samples were quickly transferred into the cavity of the scanning electron microscope without exposing them to air for long (less than 20 s). X-ray photoelectron spectroscopy (XPS) was taken to analyze the differences of the surface chemical compositions and was conducted on an Axis Ultra DLD, Kratos spectrometer using a standard Al Kα (1484.8 eV) X-ray source and an analyzer pass energy of 20 eV.

**Table S1.** The testing conditions and their corresponding labels. (The meanings of one cycle, a periodic step, shelve time and lithium dissolution time are as shown in Fig. S1.) Related to Figure 1-4.

| Label | Types of batteries | Testing mode (abbreviations) | Current density (mA $cm^{-2}$) | Total time of each charge/discharge cycle | Lithium palting time of each periodic step | Shelve time of each periodic step | Lithium dissolution time of each periodic step | Total cycle number or time | Remarks |
|---|---|---|---|---|---|---|---|---|---|
| 1M lithium bis(trifluoromethanesulfonyl)imide (LiTFSI) in 1, 3-dioxolane (DOL)/1, 2-dimethoxyethane (DME)=1:1, 1.0% $LiNO_3$ | | | | | | | | | |
| A1 | Li/Cu | CM (CM-100) | 1 | 60 min | 60 s | | | 100 cycle | Pre-depositing amount of lithium |
| A2 | Li/Cu | STCRM (STCRM-100) | 1 | 70 min | 60 s | 10 s | | 100 cycle | Same as above |
| A3 | Li/Cu | ABCM (ABCM-100) | 1 | 70 min | 60 s | | 5 s | 100 cycle(Fig. S4e)/800 h(Fig. S9) | Same as above |
| A4 | Li/Cu | STCRM | 1.154 | 60 min | 240 s | 40 s | | 100 cycle | Same as above |
| A5 | Li/Cu | ABCM | 1.154 | 60 min | 240 s | | 20 s | 100 cycle | Same as above |
| A6 | Li/Cu | STCRM | 1.165 | 60 min | 60 s | 10 s | | 100 cycle | Same as above |
| A7 | Li/Cu | ABCM | 1.165 | 60 min | 60 s | | 5 s | 100 cycle | Same as above |
| A8 | Li/Cu | STCRM | 1.2 | 60 min | 20 s | 4 s | | 100 cycle | Same as above |
| A9 | Li/Cu | ABCM | 1.2 | 60 min | 20 s | | 2 s | 100 cycle | Same as above |
| A10 | Li/Cu | CM (CM-200) | 3 | 60 min | 60 s | | | 200 cycle | Same as above |
| A11 | Li/Cu | STCRM (STCRM-200/250) | 3 | 70 min | 60 s | 10 s | | 200 cycle+50 cycle | Same as above |
| A12 | Li/Cu | ABCM (ABCM-200/250) | 3 | 70 min | 60 s | | 5 s | 200 cycle+50 cycle | Same as above |
| B1 | Li/Cu(C) | STCRM (STCRM-1000) | 1 | 70 min | 60 s | 10 s | | 1000 h | Same as above |
| B2 | Li/Cu(C) | ABCM (ABCM-1000) | 1 | 70 min | 60 s | | 5 s | 1000 h | Same as above |
| B3 | Li/Cu(C) | ABCM | 1 | 70 min | 60 s | | 5 s | 10 cycle | Same as above |
| B4 | Li/Cu(C) | ABCM | 1 | 90 min | 20 s | | 5 s | 10 cycle | Same as above |
| B5 | Li/Cu(C) | ABCM | 1 | 75 min | 40 s | | 5 s | 10 cycle | Same as above |
| B6 | Li/Cu(C) | ABCM | 1 | 65 min | 120 s | | 5 s | 10 cycle | Same as above |
| B7 | Li/Cu(C) | ABCM | 1 | 64 min | 60 s | | 2 s | 10 cycle | Same as above |
| B8 | Li/Cu(C) | ABCM | 1 | 80 min | 60 s | | 10 s | 10 cycle | Same as above |
| B9 | Li/Cu(C) | ABCM | 1 | 100 min | 60 s | | 20 s | 10 cycle | Same as above |
| C1 | Li/Li | CM | 1 | 60 min | 60 s | | | 100 cycle | |
| C2 | Li/Li | STCRM | 1 | 70 min | 60 s | 10 s | | 100 cycle | |
| C3 | Li/Li | ABCM | 1 | 70 min | 60 s | | 5 s | 100 cycle | |
| C4 | Li/Li | STCRM | 1.2 | 60 min | 20 s | 4 s | | 100 cycle | |
| C5 | Li/Li | ABCM | 1.2 | 60 min | 20 s | | 2 s | 100 cycle | |
| C6 | Li/Li | CM (CM-h) | 3 | 60 min | 60 s | | | 200 h | |
| C7 | Li/Li | ABCM (ABCM-a) | 3 | 70 min | 60 s | | 5 s | 273 h | |
| C8 | Li/Li | STCRM (STCRM-h) | 3.6 | 60 min | 20 s | 4 s | | 200 h | |
| C9 | Li/Li | ABCM (ABCM-h/b) | 3.6 | 60 min | 20 s | | 2 s | 200 h( Fig. 3b) /534 h(Fig. S25) | |
| 1M $LiPF_6$ in EC/DMC/DEC=1:1:1 | | | | | | | | | |
| D1 | Li/Cu(C) | CM | 1 | 60 min | 60 s | | | around 85 h | Pre-depositing amount of lithium |
| D2 | Li/Cu(C) | ABCM | 1 | 80 min | 60 s | | 10 s | around 100 h | Same as above |
| E1 | Li/Li | CM | 0.5 | 60 min | 60 s | | | 150 h | |
| E2 | Li/Li | STCRM | 0.5 | 80 min | 80 s | 20 s | | 150 h | |
| E3 | Li/Li | ABCM | 0.5 | 80 min | 80 s | | 10 s | 150 h | |

**Time-Current Curve:**

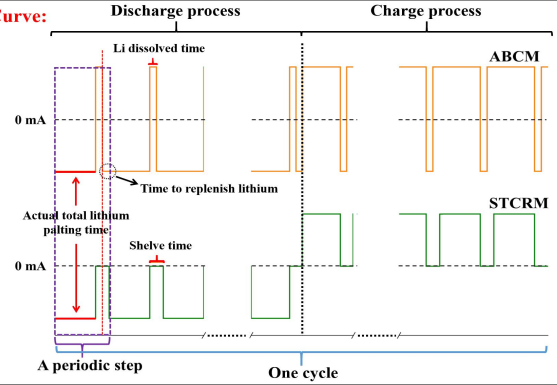


Noting:
1.The lithium plating time of each periodic cycle described in the table is the actual deposition time of lithium after the dissolution time , and the shelving time in STCRM is split into half dissolved and half replenished in ABCM;
2.Some other test details are described in the article.

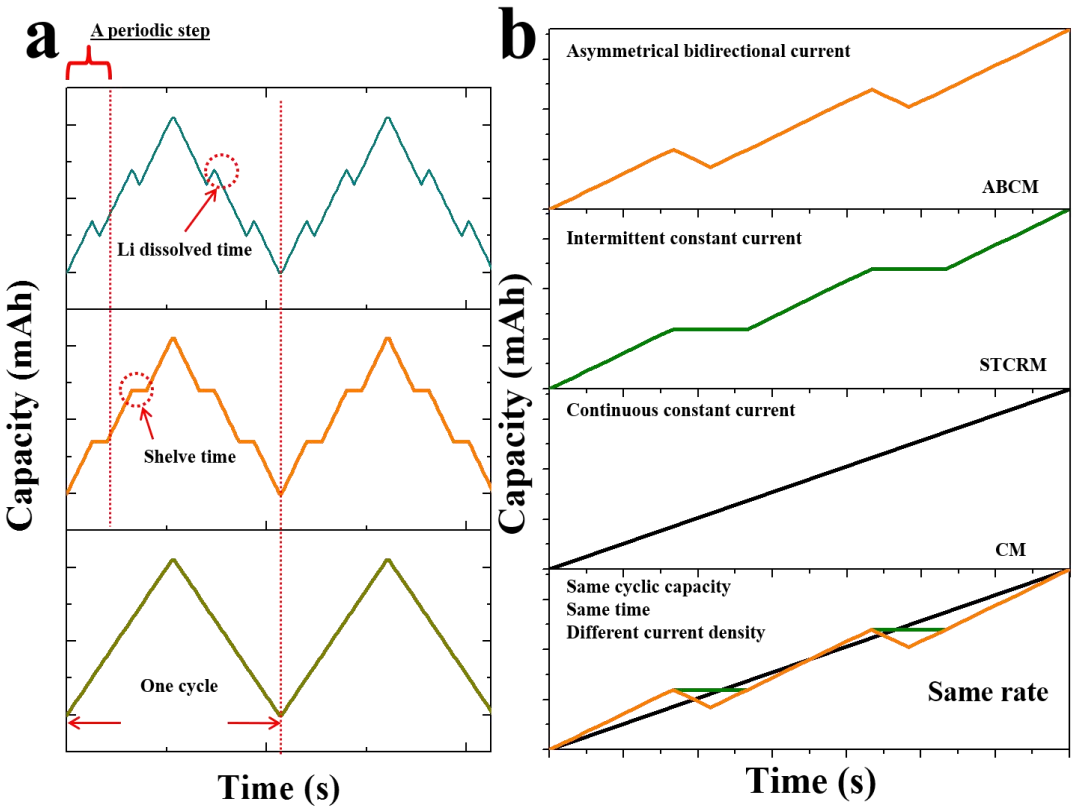


Figure S1. (a) The different profiles of the three charging modes under the conditions of same time and cycle capacity. One cycle, as labeled at the bottom, contains a constant plating or stripping Li. Meanwhile, a periodic step means a periodic plating Li with a periodic shelve time or Li dissolved time in every half cycle. In order not to affect the total plating or stripping Li source, the dissolving time is set only half of shelve time. (b) The profiles of the applied current of three charging modes at the same rate (same cyclic capacity and same time). Related to Figure 1.

Please note Figure S1b is different from the schematic diagram shown in Figure 1a. Figure 1a shows a same cyclic capacity and same current density, under the condition of Figure 1a, STCRM and ABCM will cost more time to compensate the capacity loss caused by the shelved time and anti-current time.

As shown in Fig. S1, at the same rate condition (same time and same capacity at each cycle), STCRM and ABCM will need a higher current density in the premise of ensuring the same rate. And the current density is calculated on the actual lithium plating capacity and total time (t), t includes the real Li plating time and shelve time/healing time.

Those schematic diagrams mainly base on symmetric battery. During each cycle, one electrode is plating Li, and meanwhile another electrode is stripping Li. Therefore we use ABCM or STCRM way at both charging and discharging process. In addition, for the full battery (Li/LCO), we use ABCM as charge process (Li plating) and CM as discharge process (Li stripping).

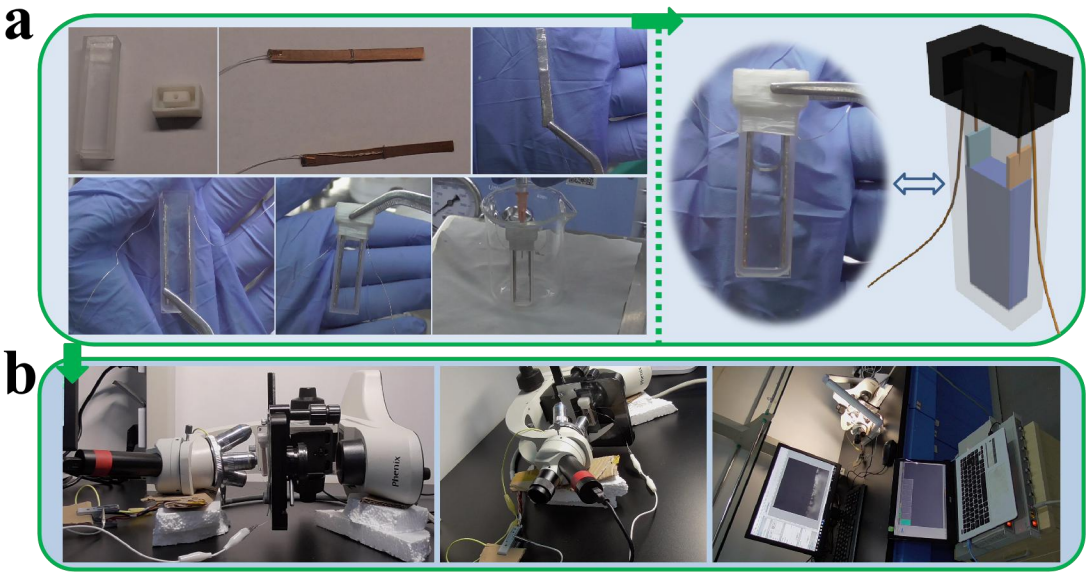


Figure S2. (a) A schematic diagram and photograph of the electrolytic cell. (b) A photograph of the electrolytic in-situ electrochemical visual battery. Related to Figure 2.

Herein, when we use ABCM way to deposited Li metal, we chose the same current density as CM way for comparison. In other experiments, in order to get a clearer view of healing process, the dissolution condition is optimized (the time and current density).

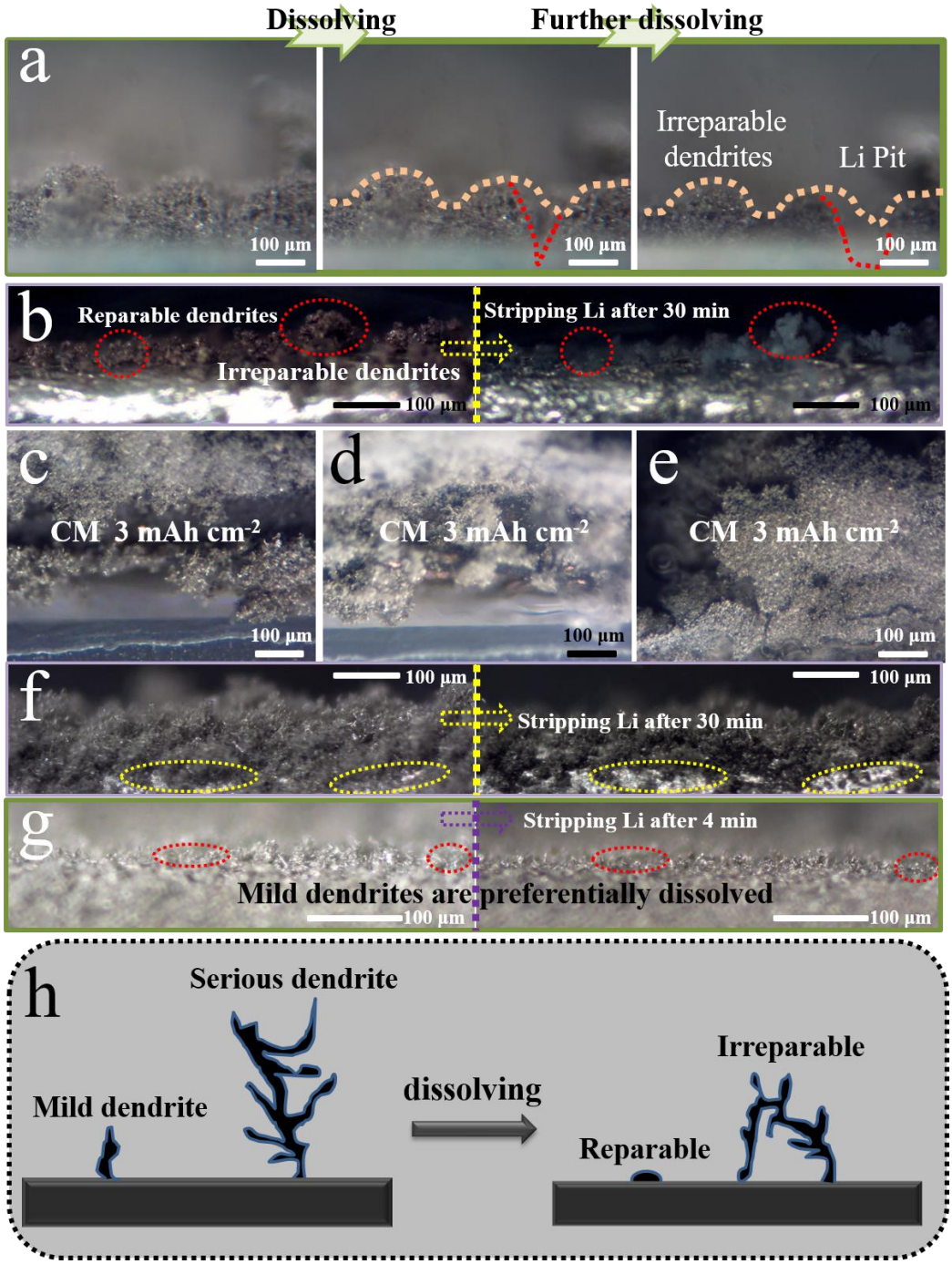


Figure S3. (a) In-situ electrochemical visual battery in carbonate based electrolyte for dendrite dissolving behavior at 5 mA $cm^{-2}$ using Li/Cu battery. (b) Different dendrite dissolving behaviors: mild dendrite and serious dendrite using Li/Li battery in carbonate based electrolyte. (c)/(d)/(e) Different areas of plated Li at 3 mAh $cm^{-2}$ using CM way and Li/Cu battery with chaotic dendrites in carbonate based electrolyte. (f) and (g) In-situ electrochemical visual battery in ether based electrolyte for dendrite dissolving behavior. (h) Schematic diagram to exhibit the difference between serious and mild dendrites. Related to Figure 2 and Video S1-6.

The difference of "mild" and "serious" dendrites are caused by the charging current density and charging time: As we know, in the electrolyte, the $Li^+$ concentration obeys an effective diffusion

equation(Newman and Thomas, 2004). During the electrochemical reaction process, the concentration of $Li^+$ is changing as a dynamic process. When currents exceed diffusion limitation, the concentration of $Li^+$ on the electrode surface decreases to zero at a characteristic time, which causes an unstable and no-uniform electroplating. This characteristic time is named as $t_{Sand}$, after this $t_{Sand}$, the scarce supply of cations preferentially deposits onto surface protrusions, leading to a self-amplifying process of dendritic growth, which we called the "serious" dendrites. The $t_{Sand}$ is defined by the Sand's formula(Sand, 1901):

$$t_{Sand} = \pi D_{app} \frac{\left(Z_c C_0 F\right)^2}{4\left(J t_a\right)^2}$$

where $Z_c$ is the charge number of the cation, $C_0$ is the bulk salt concentration, F is the Faraday's constant, J is the current density, and $t_a$ is the transference numbers of lithium cations and associated anions. From this formula we can see that the larger J, the shorter $t_{Sand}$, which means the easier to reach the "serious" dendrites.

Fig. S3h shows that vertical columnar dendrite ("mild" dendrite) would be easy to be corrected, while branch dendrite ("serious" dendrites) would be difficult to be repaired. It may be result from branch dendrite owns disordered electric field distribution or chaotic current density distribution, discussed in the literature(Wood et al., 2016; Yang et al., 2015). This phenomenon can intuitively be seen through in-situ batteries, including Figure 2/Figure3a-g/Video1-6, especially in Fig. 2a and 2b, a columnar dendrite (beyond 100 μm) can be repaired while the branch morphology dendrite cannot be repaired. The corresponding data were shown in Figure 3b/d and S25, which make the comparison more clear.

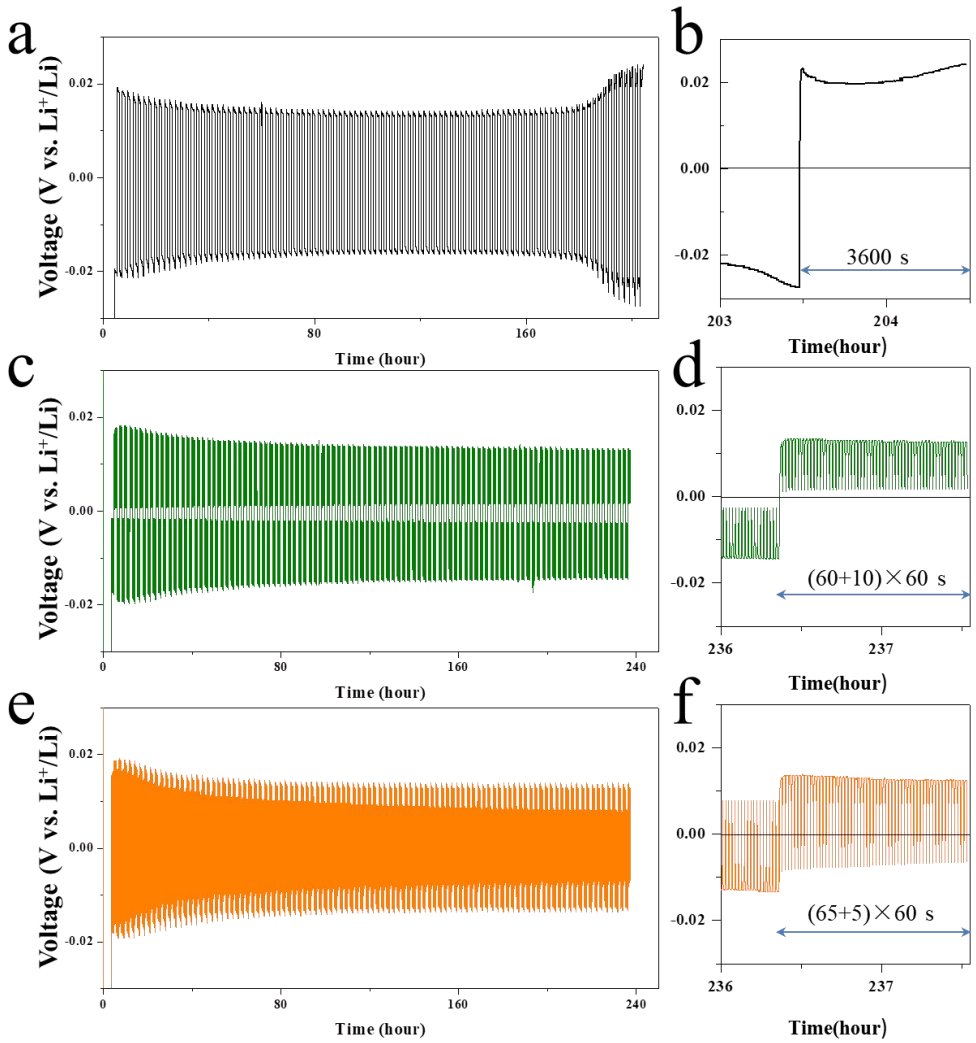


Figure S4. Polarization of Li symmetric battery (pre-deposition excess Li on copper at the same condition), (a)/(c)/(e) CM, STCRM and ABCM for 100 cycles at 1 mA $cm^{-1}$/1 mAh $cm^{-1}$ respectively (STCRM-100 means 10 seconds shelve per 70 seconds; ABCM-100 is 5 seconds anti-direction current per 70 seconds, see A1-A3 in table S1). (b)/(d)/(f) Enlarged views of voltage profile of tree type modes at $100^{th}$ cycle, CM, STRCM and ABCM from top to down in order. Related to Figure 4.

Figure S4b/d/f show the charge processes of CM, STCRM and ABCM lasting 3600/4200/4200 seconds respectively.

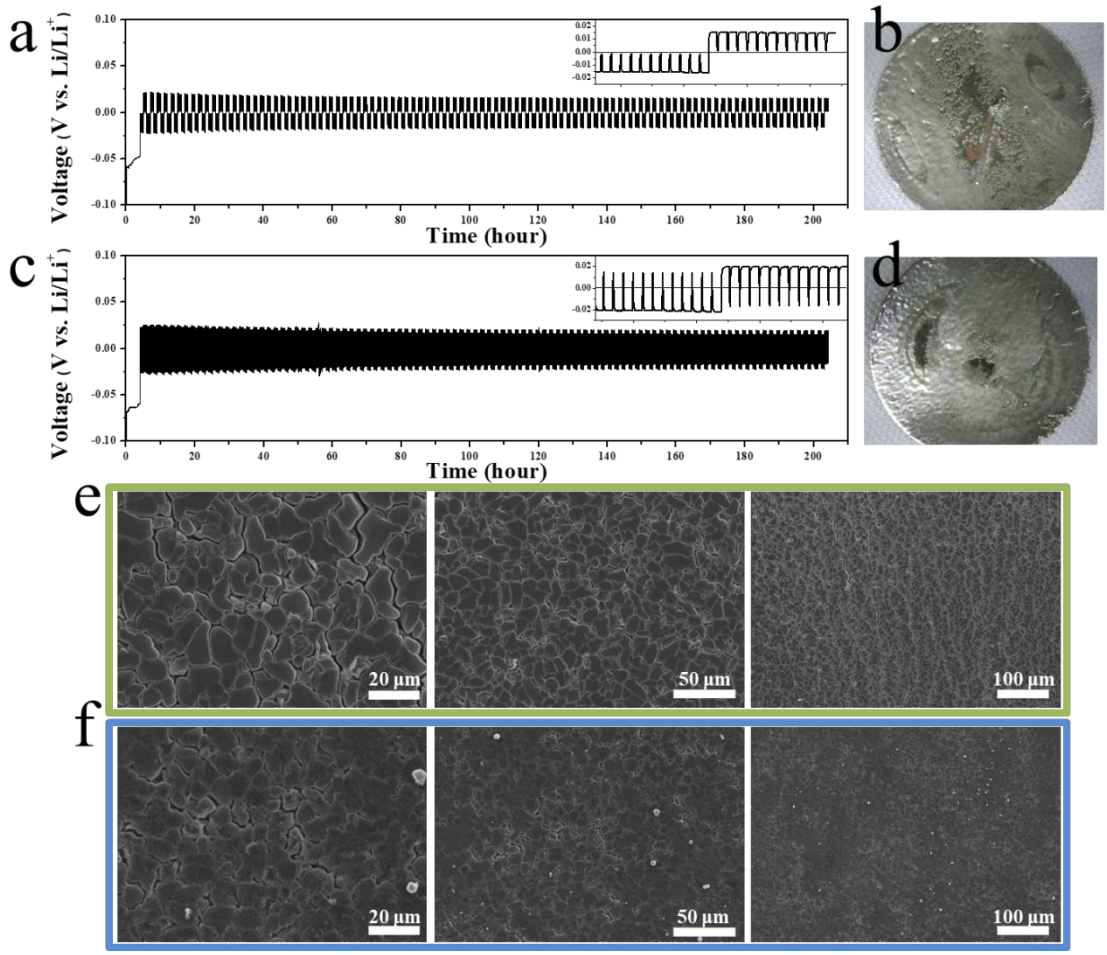


Figure S5. (a) Polarization of Li symmetric battery using STCRM route at 1 mAh $cm^{-2}$ and 1.154 mA $cm^{-2}$ (see A4 in table S1). (b) Photograph of copper-side electrode for (a). (c) Polarization of Li symmetric battery using ABCM route at 1 mAh $cm^{-2}$ and 1.154 mA $cm^{-2}$ (see A5 in table S1). (d) Photograph of copper-side electrode for (c). (e) SEM of (b). (f) SEM of (d). Related to Figure 4.

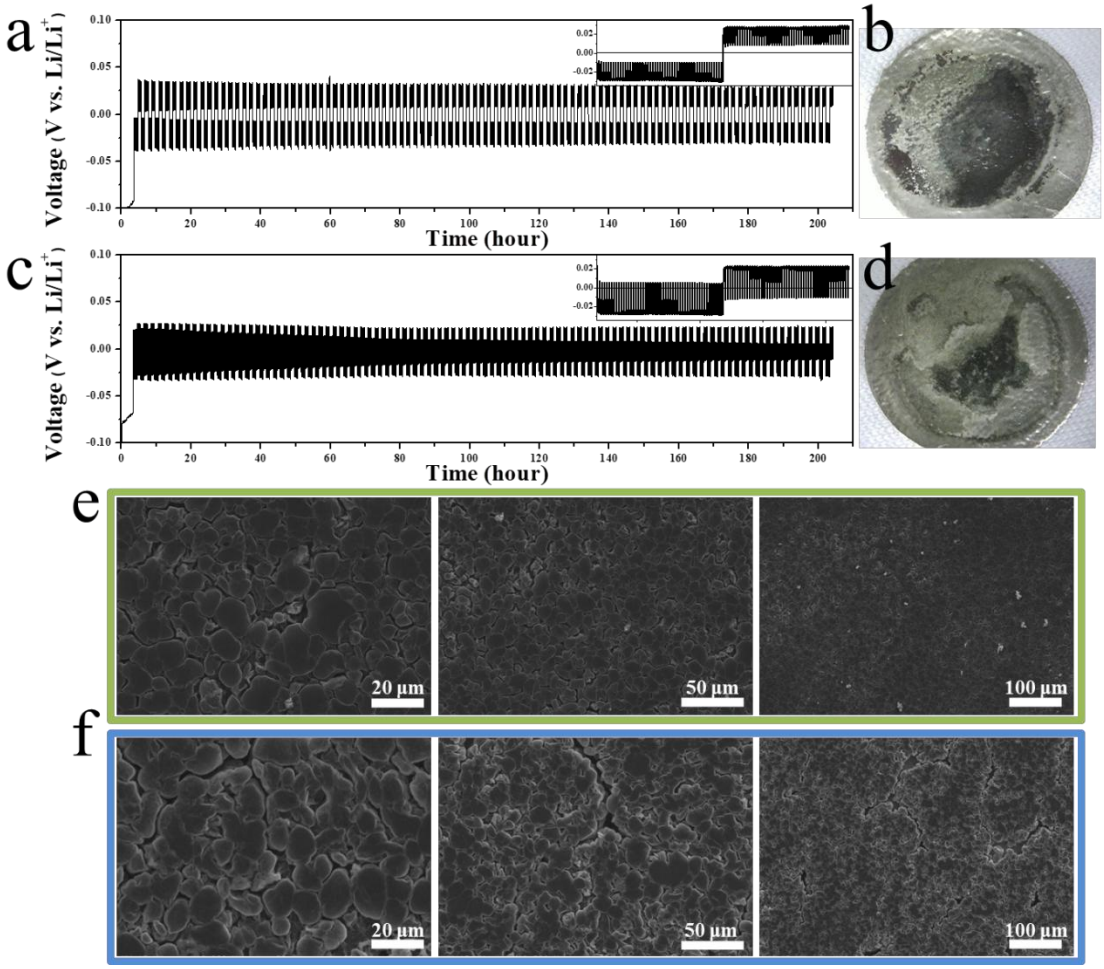


Figure S6. (a) Polarization of Li symmetric battery using STCRM route at 1 mAh/cm$^2$ and 1.165 mA/ cm$^2$ (see A6 in table S1). (b) Photograph of copper-side electrode for (a). (c) Polarization of Li symmetric battery using ABCM route at 1 mAh/cm$^2$ and 1.165 mA/ cm$^2$ (see A7 in table S1). (d) Photograph of copper-side electrode for (c). (e) SEM of (b). (f) SEM of (d). Related to Figure 4.

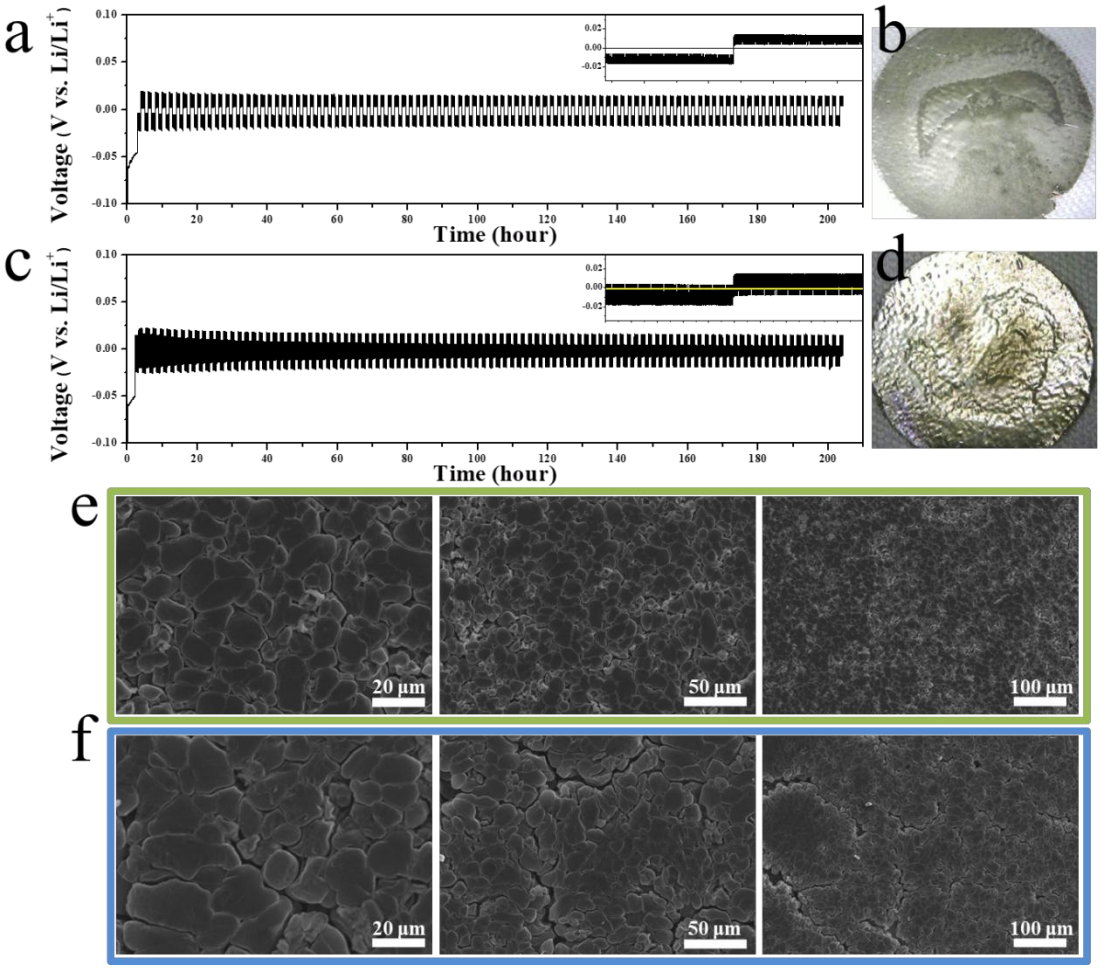


Figure S7. (a) Polarization of Li symmetric battery using STCRM route at 1 mAh/cm$^2$ and 1.2 mA/ cm$^2$ (see A8 in table S1). (b) Photograph of copper-side electrode for (a). (c) Polarization of Li symmetric battery using ABCM route at 1 mAh/cm$^2$ and 1.2 mA/ cm$^2$ (see A9 in table S1). (d) Photograph of copper-side electrode for (c). (e) SEM of (b). (f) SEM of (d). Related to Figure 4.

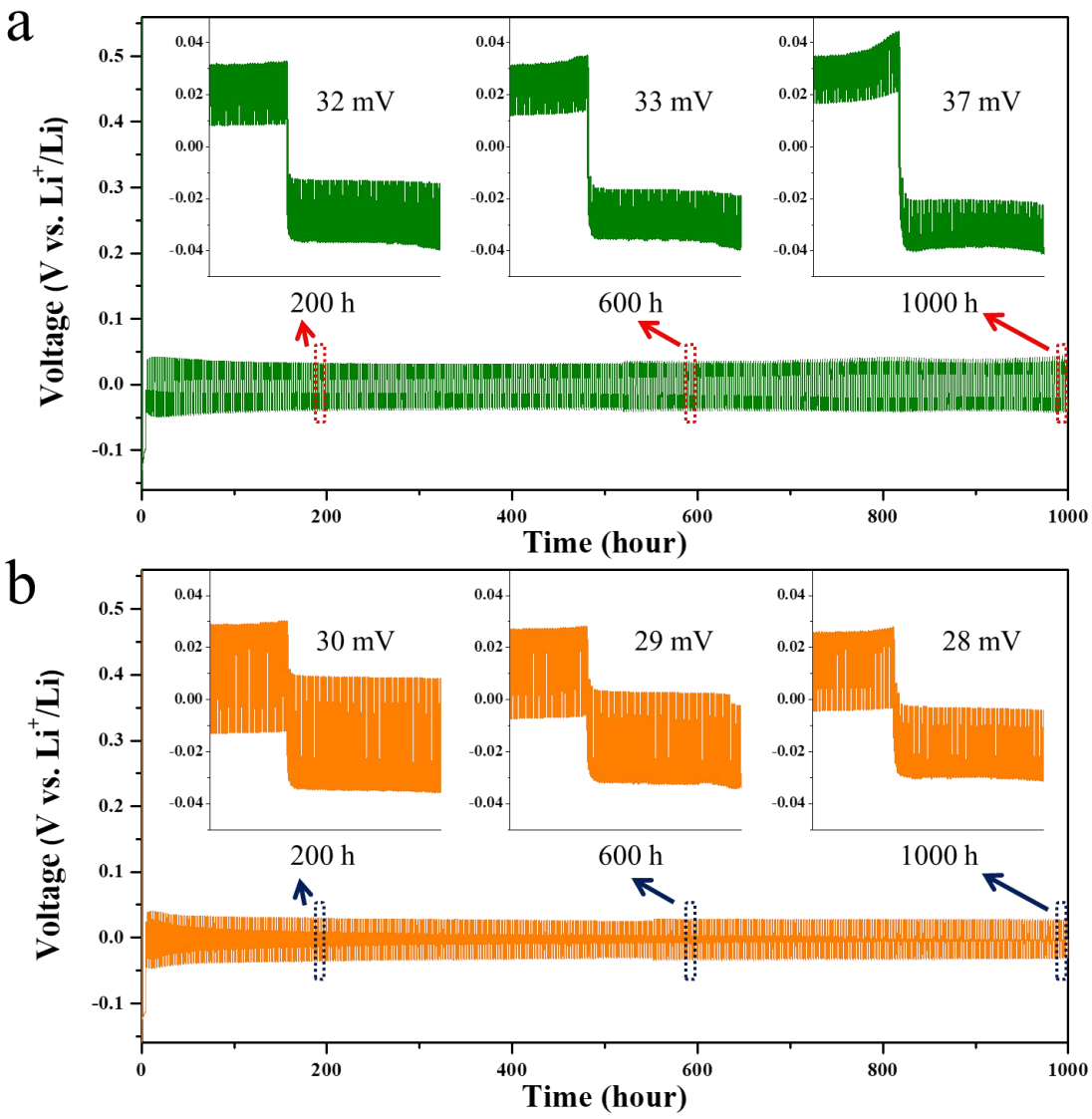


157

158 Figure S8. Detailed voltage profiles of 200$^{th}$ 600$^{th}$ and 1000$^{th}$ hour for STCRM-1000 ((a), see B1 in
159 table S1) and ABCM-1000 ((b), see B2 in table S1) using Li/carbon coating copper batteries. Related to
160 Figure 3.

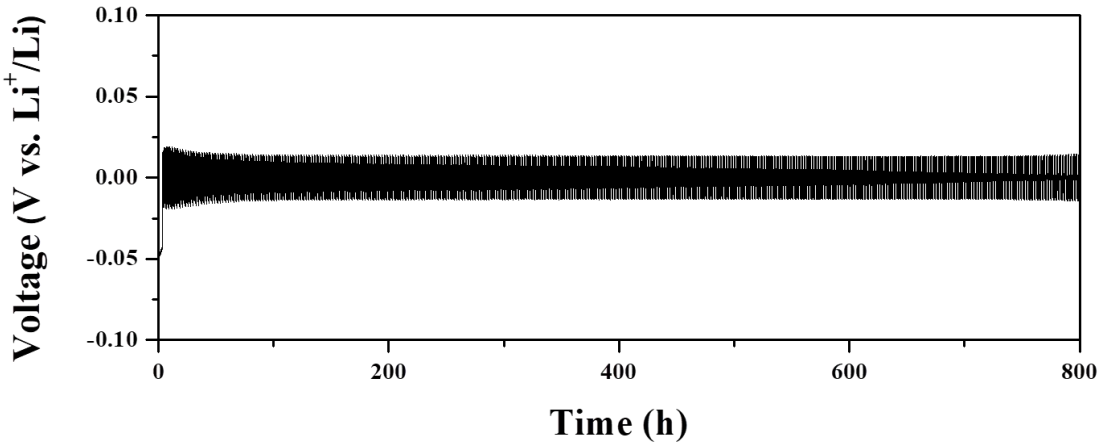


161

162 Figure S9. Long cyclic polarization for Li-Cu battery system (see A3 in table S1). Related to Figure 3.

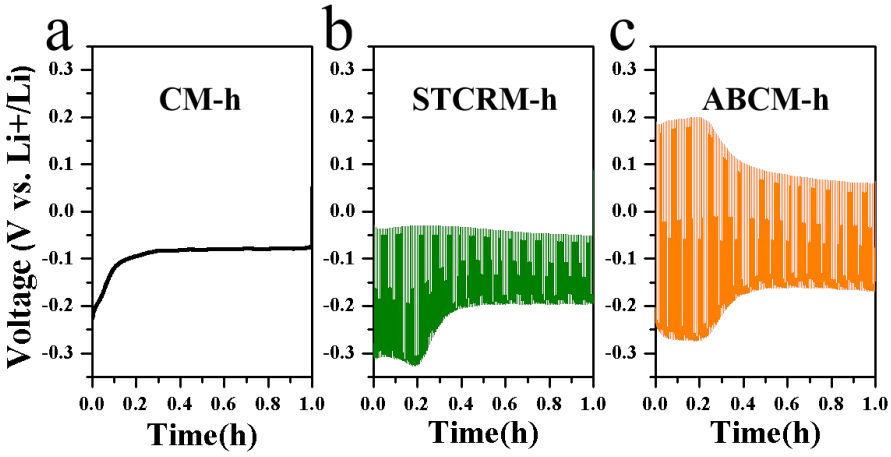


Figure S10.The initial polarization of Li/Li symmetric batteries ((a) CM-h, (b) STCRM-h, and (c) ABCM-h) for 200 hours at and 3 mAh $cm^{-2}$. Related to Figure 3.

Since the current density of CM-h is 3 mA $cm^{-2}$, whereas the current density of STCRM-h and ABCM-h is 3.6 mA $cm^{-2}$ (the aim is to compare the three types of charge-discharge modes at the same time and capacity), CM-h has a lower initial polarization. Interestingly, both ABCM-h and STCRM-h exhibit an obvious reducing overpotential, which may be originated from initial SEI optimization, surface Li ion flux, nucleation and other reasons. Noteworthy, STCRM-h have obvious nucleation barrier, while ABCM-h do not. It indicates that the Li plating would be more stable if ABCM-h is used(Fan et al., 2018; Pei et al., 2017).

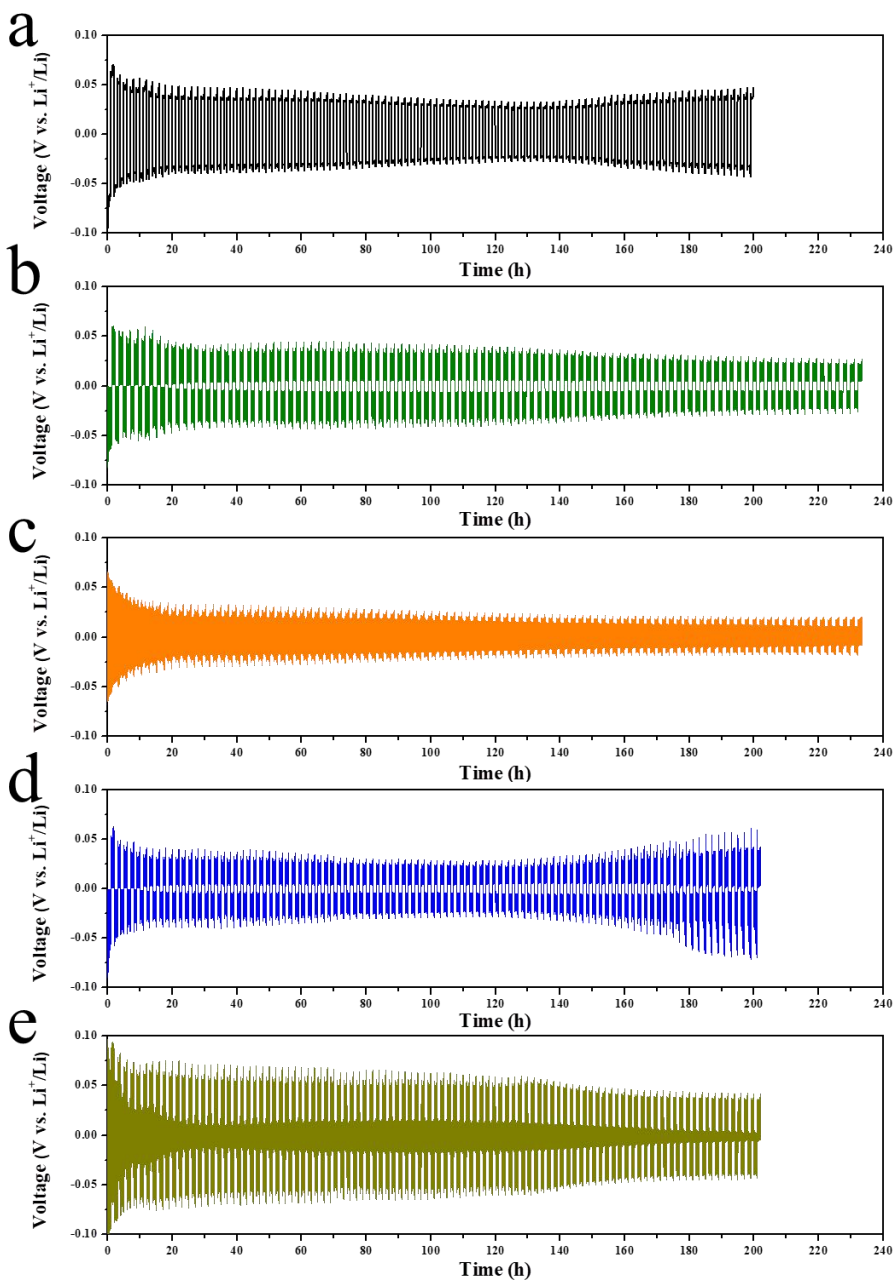


Figure S11. 100-cycles polarization of Li symmetric battery (Li foil/Li foil). a/b/c/d/e are C1/C2/C3/C4/C5 in table S1, respectively. Related to Figure 3.

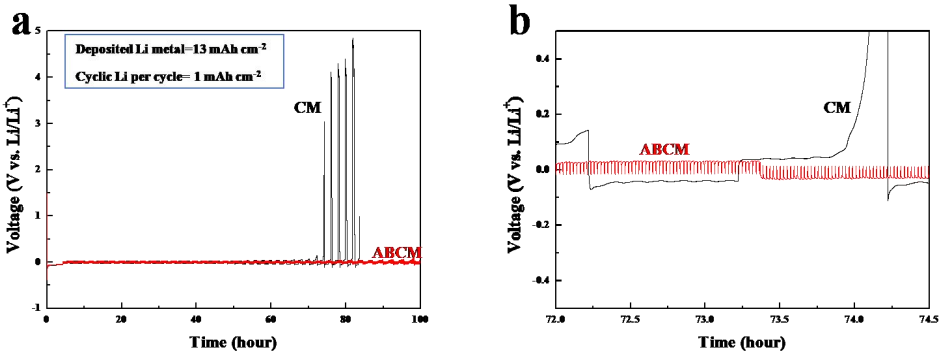


177

178 Figure S12. polarization of Li symmetric battery in carbonate based electrolyte for ABCM and CM. (a)
179 100 hour and (b) detail from 72 to 74.5 hour. See D1, D2 in table S1. Related to Figure 3.
180

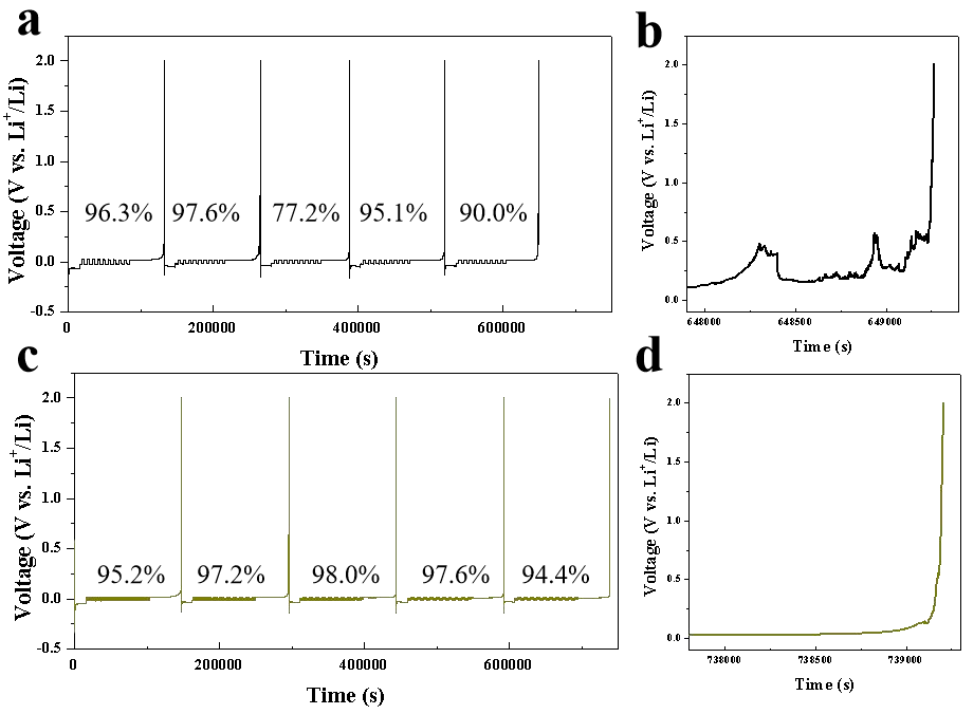


Figure S13. C.E.s of CM and ABCM, (a)/(b) detailed voltage profile and C.E. of CM (the same as A1) and ABCM (the same as A3), respectively. (c)/(d) final voltage profile of Li metal stripping for CM and ABCM, respectively. Related to Figure 3.

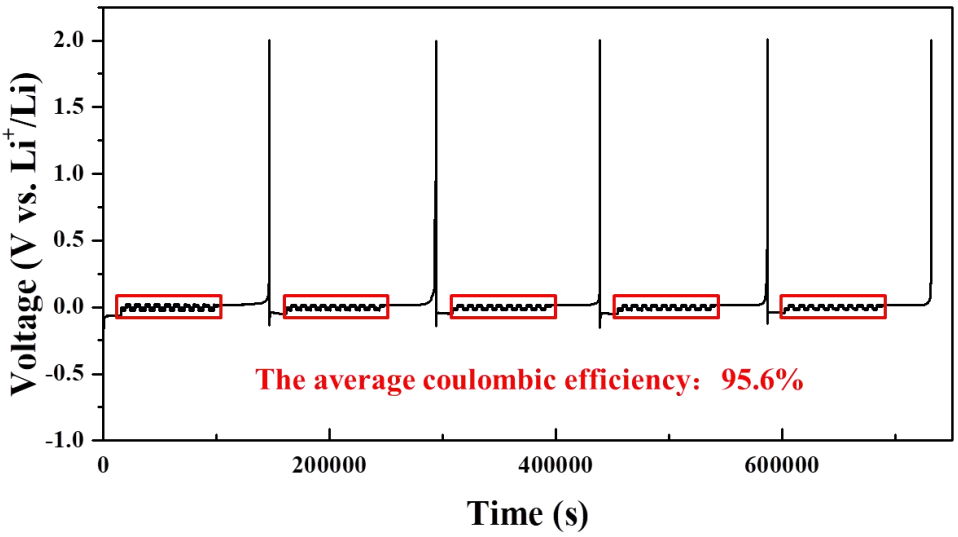


185

186 Figure S14. Detailed voltage profile and C.E. of STCRM, after deposited the same amount of Li on
187 carbon coated copper, then after 10 loops of STCRM (the same as A2). Related to Figure 3.
188
189 Hypothetically pre-deposited Li metal owns 100% C.E. (pre-deposited Li metal on copper involved
190 interface heterogeneous nucleation and this part of Li metal also affect the true C.E.), thereof, for 50
191 cycles the average C.E. of STCRM can be gained as 95.60%(Cheng et al., 2017).

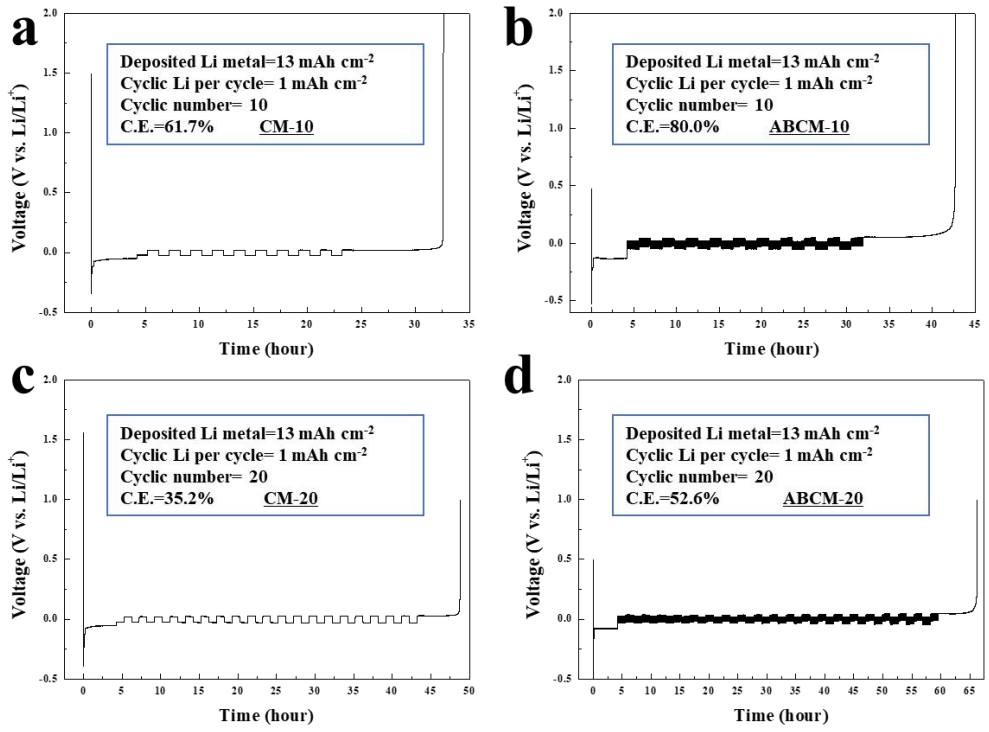


192

193 Figure S15. Detailed voltage profile and C.E. of CM and ABCM in carbonate based electrolyte. (a), 10
194 loops of CM, (b), 10 loops of ABCM, (c), 20 loops of CM, (d), 20 loops of ABCM. Related to Figure 3.

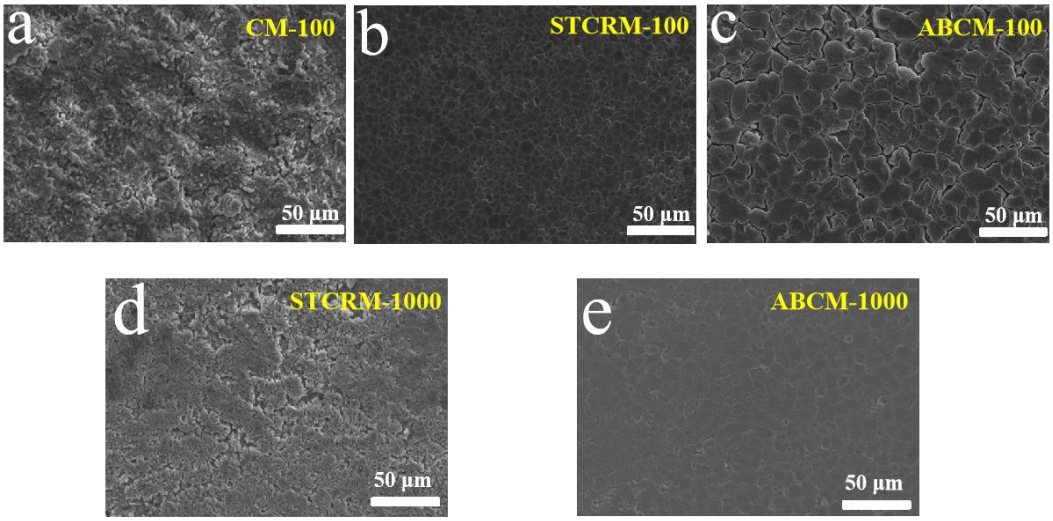


195

196 Figure S16. SEM of (a) CM-100 (A1), (b) STCRM-100 (A2), (c) ABCM-100 (A3), (d) STCRM-1000
197 (B1), and (e) ABCM-1000 (B2). Related to Figure 4.

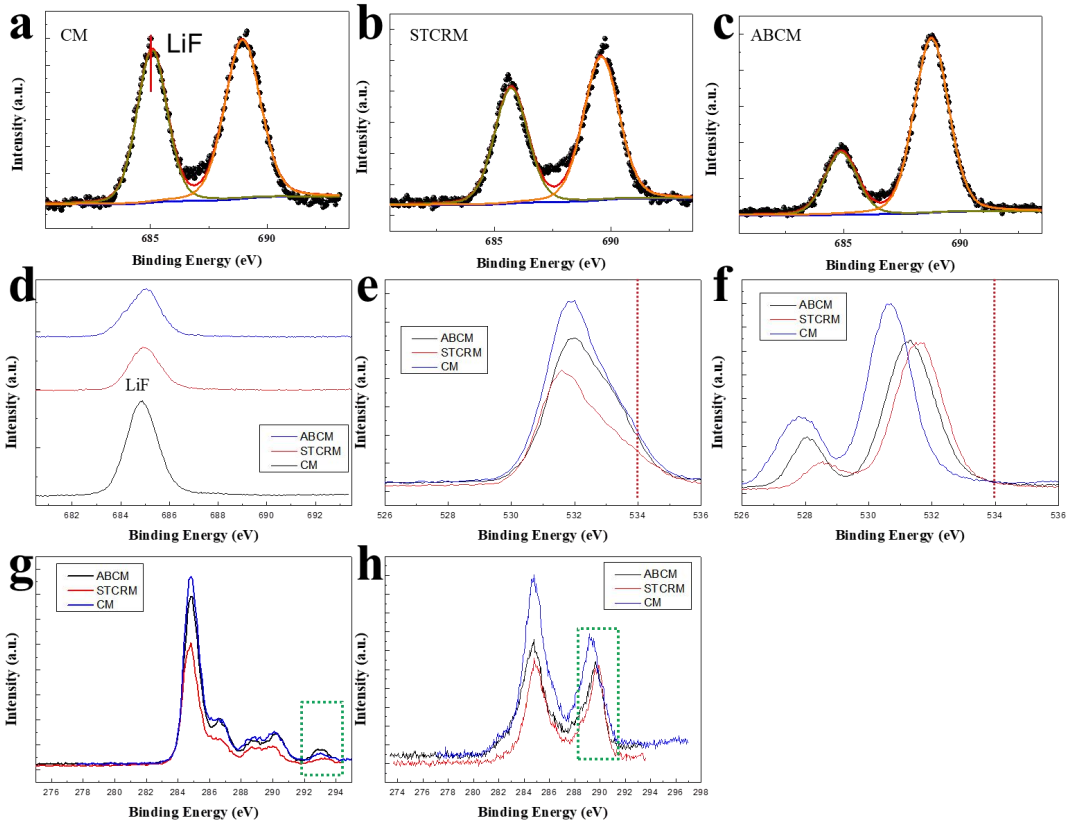


Figure S17. The F1s peak fitting of CM (a) STCRM (b) and ABCM (c). (d) F1s peaks of these three routes after Ar ion etching. (e), (f) O1s peaks of three routes before/after Ar ion etching, respectively. (g) (h) O1s peaks of three routes before/after Ar ion etching, respectively. Related to Figure 4.

As show in Figure S17 a-c, the peak at ~around 688 eV is F based band in organic content. Figure S17e shows the peak in ~534 eV and ~529 eV may be the C-O and C=O band in organic SEI film. As shown in Figure S17 g, the peak at ~293 eV may be C-F band in organic SEI layer, the peak 286 eV and 288 eV may be C-O and C=O band in organic SEI layer. As shown in Figure S17 d/f/h, the organic content in SEI film is rare, indicating pure inorganic content in SEI film(Eshkenazi et al., 2004).

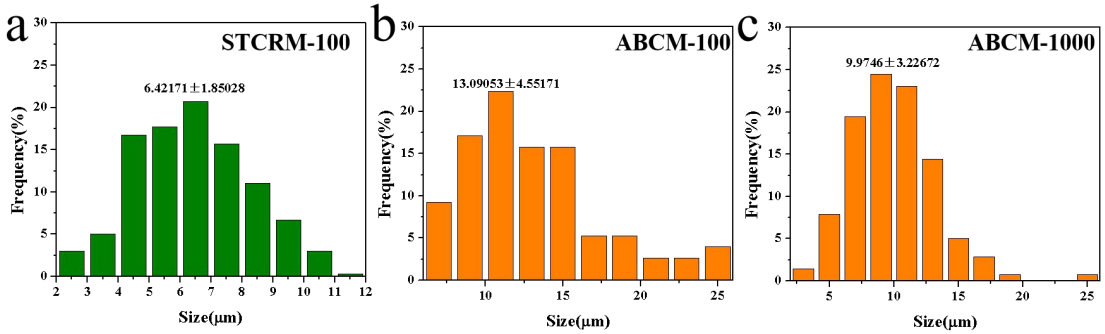


Figure S18. The size distribution of (a) STCRM-100 (A2), (b) ABCM-100 (A3), and (c) ABCM-1000 (B2). Related to Figure 4.

Herein, the particle size distribution is obtained by using particle size distribution calculation software—Nano Measurer 1.2.0 (Xu jie, laboratory of surface chemistry and catalysis, department of chemistry, Fudan University). We also used the corresponding SEM image into the software and manually selected statistical samples for calculation according to the rule.

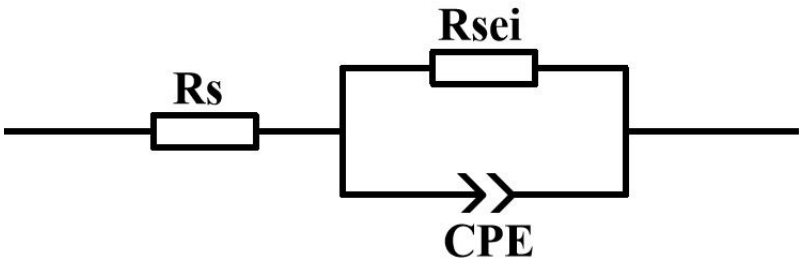


Figure S19. Equivalent circuit of Li metal battery, Rs means natural impedance of electrolyte and electrode, and Rsei is the impedance of SEI film coating on Li metal. CPE is constant phase element, which is a supplement for Rsei. Related to Figure 4.

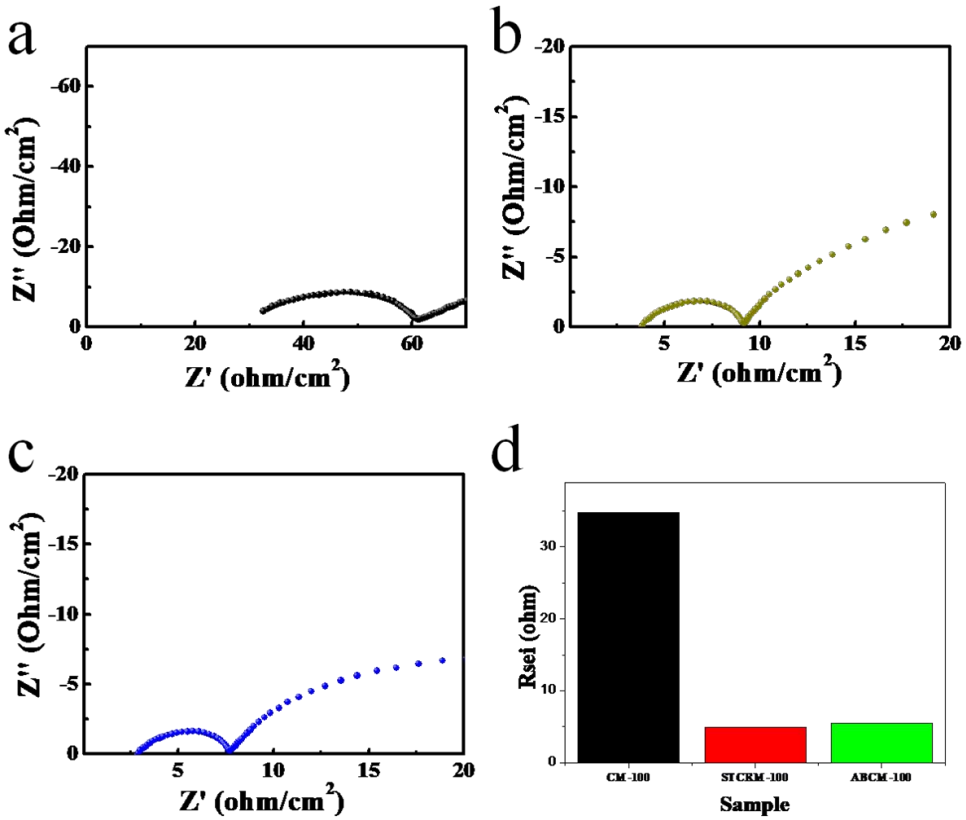


220

221 Figure S20. The impedances of these samples, (a) CM-100 (A1), (b) STCRM-100 (A2), (c)
222 ABCM-100 (A3), (d) Rsei of these samples. Related to Figure 4.

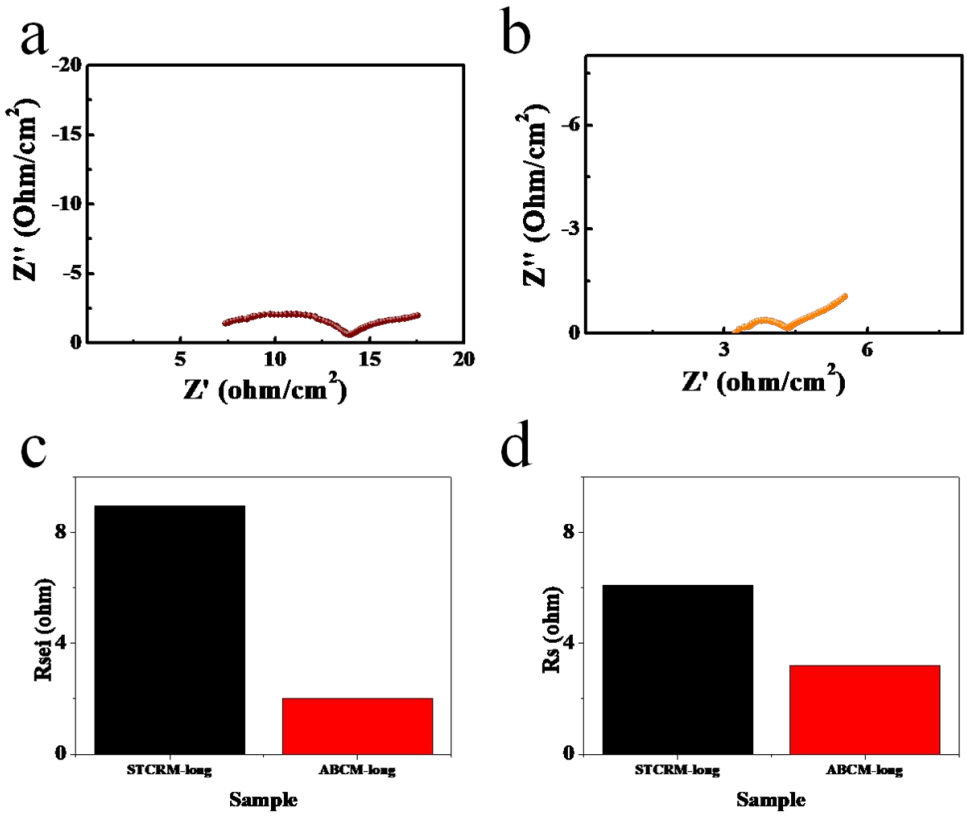


Figure S21. The impedances of the samples, (a) STCRM-1000 (B1), (b) ABCM-1000 (B2), (c) Rsei of these samples, (d) Rs of these samples. Related to Figure 4.

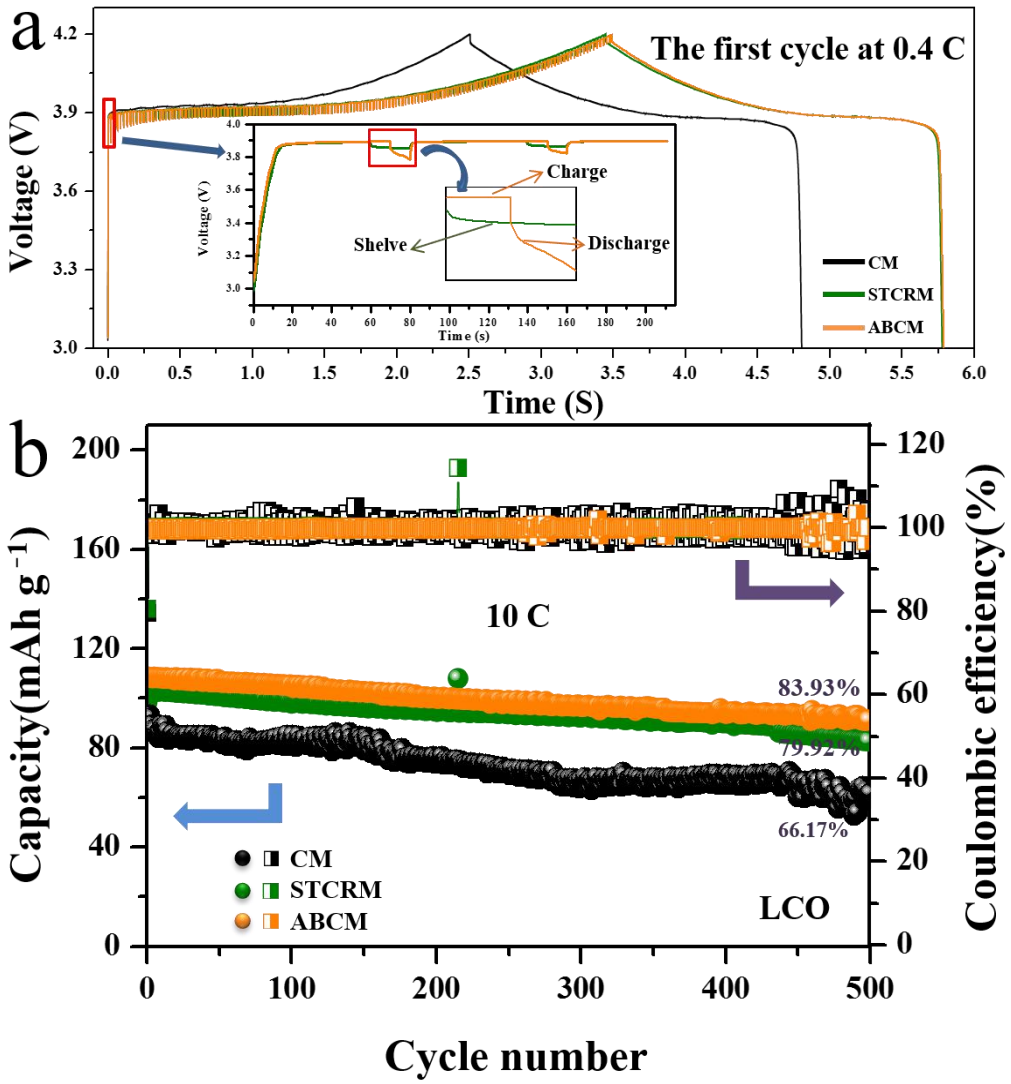


Figure S22. (a) Detailed time-voltage curve of the first cycle at 0.4 C for CM, STCRM and ABCM using Li/$LiCoO_2$ batteries, which corresponds to Figure 4h. (b) Long term stability of CM, STCRM and ABCM at 10 C for Li/$LiCoO_2$ batteries. (The specific charging and discharging process is the same as that in Figure 4h and Figure S22a. The full circles represent the specific discharge capacity, and the half squares represent the Coulombic Efficiency.) Related to Figure 4.

As shown in Fig. S22a, we show this to illustrate the charging and discharging patterns for full batteries. (For STCRM, 20 s shelving per 60 s charging during charging process, in contrast with 10 s discharging per 70 s charging during the charging process for ABCM. Both STCRM and ABCM use constant current as the discharging process. More details can be seen in the illustration.)

Herein, for CM and STCRM, C.E.s can be given directly by Neware battery testing system, which were calculated by $C_{(discharge\ capacity)}/C_{(charge\ capacity)}$, where the $C_{(discharge\ capacity)}$ is the discharge capacity and $C_{(charge\ capacity)}$ is the charge capacity. For ABCM, we got the actual specific charge capacity ($C_{ac}$) by $C_{ac}= C_t-C_d$, where $C_t$ is the total charge capacity, $C_d$ is the total capacity while the Li dendrite dissolving during the charging process of each cycle, and the actual specific discharge capacity ($C_{ad}$) were also given directly by Neware battery testing system. Then C.E. of ABCM is $C_{ad}/C_{ac}$.

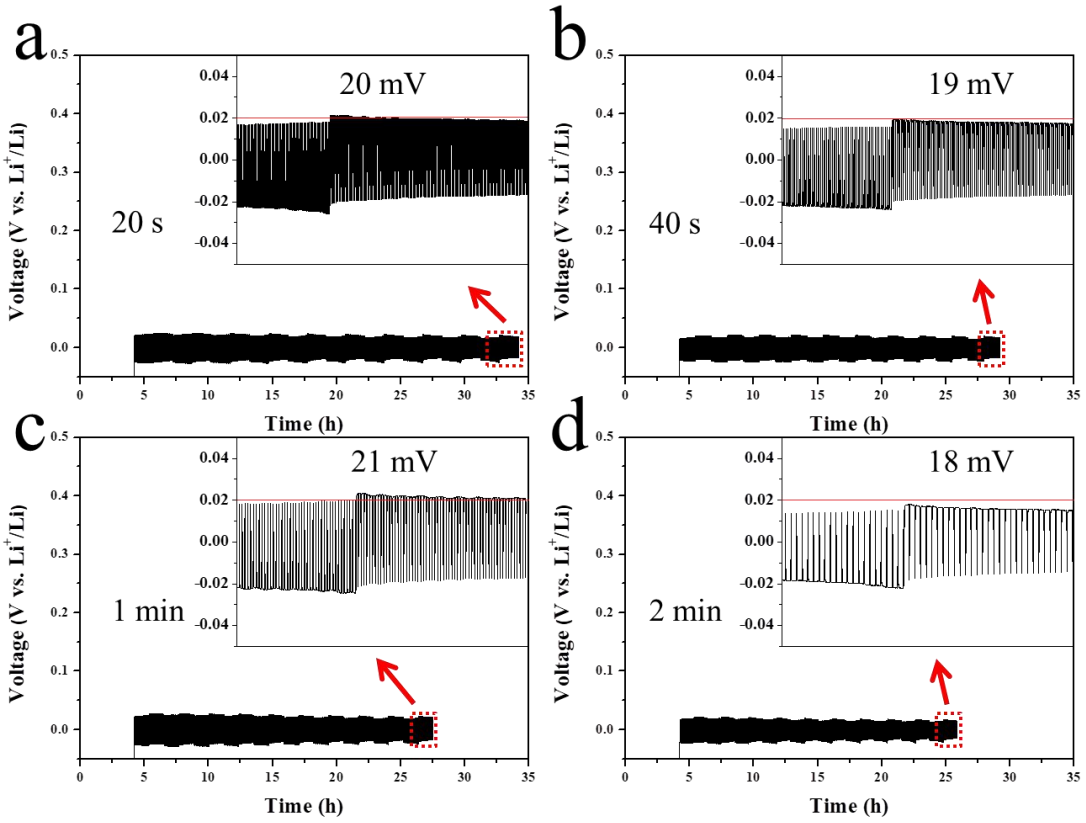


Figure S23. Different Li plating time in charge/discharge process (5 sec charge and 5 sec discharge to eliminate dendrite), (a) 20 s for plating Li, (b) 40 s for plating Li, (c) 60 s for plating Li, (d) 120s for plating Li. a/b/c/d are B4/B5/B3/B6 in table S1, respectively. Related to Figure 3.

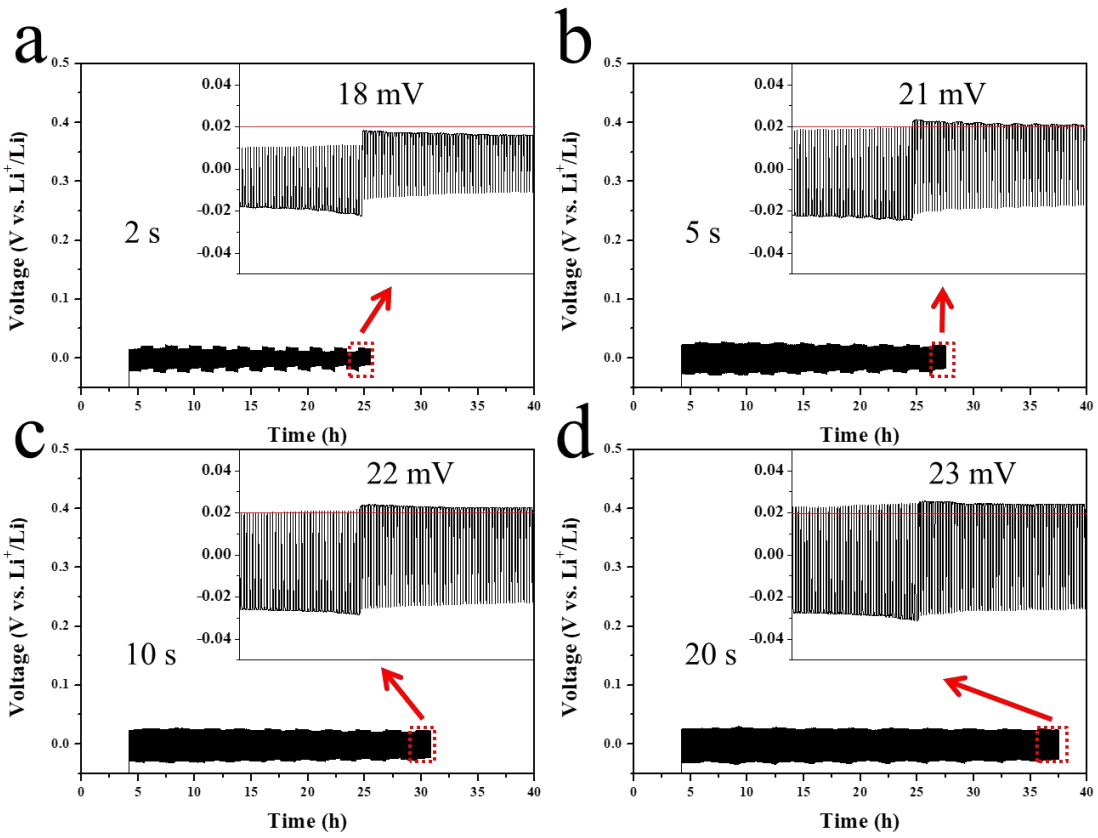


Figure S24. Different Li dissolved time in charge/discharge process (60 min for Li plating), (a) 2 s for Li dissolution, (b) 5 s for Li dissolution, (c) 10 s for Li dissolution, (d) 20s for Li dissolution. a/b/c/d are B7/B3/B8/B9 in table S1, respectively. Related to Figure 3.

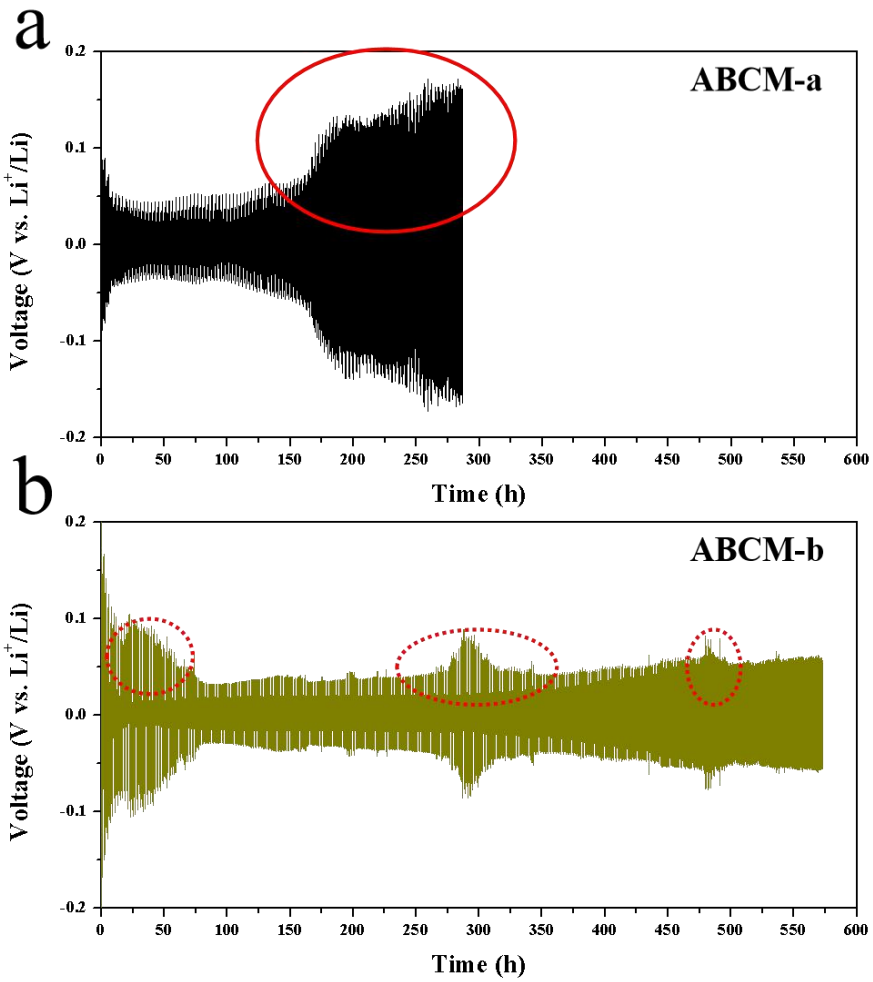


252

253 Figure S25. A polarization of different plating/dissolving at 3 mAh/cm$^2$, (a) ABCM-a (C7 in table 1), (b)
254 ABCM-b (C9 in table S1). Related to Figure 3.

# Supplemental Reference：


Cheng, X.-B., Zhao, M.-Q., Chen, C., Pentecost, A., Maleski, K., Mathis, T., Zhang, X.-Q., Zhang, Q., Jiang, J., and Gogotsi, Y. (2017). Nanodiamonds suppress the growth of lithium dendrites. Nat. Commun. *8*, 336.

Eshkenazi, V., Peled, E., Burstein, L., and Golodnitsky, D. (2004). XPS analysis of the SEI formed on carbonaceous materials. Solid State Ionics *170*, 83-91.

Fan, L., Li, S., Liu, L., Zhang, W., Gao, L., Fu, Y., Chen, F., Li, J., Zhuang, H.L., and Lu, Y. (2018). Enabling Stable Lithium Metal Anode via 3D Inorganic Skeleton with Superlithiophilic Interphase. Adv. Mater. *8*, 1802350.

Liu, H., Cheng, X.-B., Xu, R., Zhang, X.-Q., Yan, C., Huang, J.-Q., and Zhang, Q. (2019). Plating/Stripping Behavior of Actual Lithium Metal Anode. Adv. Energy Mater., Doi:10.1002/aenm.201902254.

Newman, J.S., and Thomas, K.E. (2004). Electrochemical Systems, 3rd edition. John Wiley & Sons, Hoboken, NJ.

Pei, A., Zheng, G., Shi, F., Li, Y., and Cui, Y. (2017). Nanoscale Nucleation and Growth of Electrodeposited Lithium Metal. Nano Lett. *17*, 1132-1139.

Sand, H.J.S. (1901). III. On the concentration at the electrodes in a solution, with special reference to the liberation of hydrogen by electrolysis of a mixture of copper sulphate and sulphuric acid. Philos. Mag. *1*, 45-79.

Wood, K.N., Kazyak, E., Chadwick, A.F., Chen, K.-H., Zhang, J.-G., Thornton, K., and Dasgupta, N.P. (2016). Dendrites and Pits: Untangling the Complex Behavior of Lithium Metal Anodes through Operando Video Microscopy. ACS Cent. Sci. *2*, 790-801.

Yang, C.-P., Yin, Y.-X., Zhang, S.-F., Li, N.-W., and Guo, Y.-G. (2015). Accommodating lithium into 3D current collectors with a submicron skeleton towards long-life lithium metal anodes. Nat. Commun. *6*, 8058.